Stockholm
University

Numerical approaches to droplet growth in atmospheric turbulence

Xiang-Yu Li

Supervisor at Nordita: Prof. Axel Brandenburg

Supervisor at Stockholm University: Prof. Gunilla Svensson

Department of Meteorology, Stockholm University

Licentiate thesis in Atmosphere Sciences and Oceanography, Sweden, 2016

Cover image: A view of the clouds taken at Sandhamn, Sweden.

Photo by: Xiang-Yu Li

ISBN 978-91-7649-440-0

Printed in Sweden by E-print AB, Stockholm 2016
Distributor: Department of Meteorology, Stockholm University

Abstract

The bottleneck problem of cloud droplet growth is one of the most challenging problems in cloud physics. Cloud droplet growth is neither dominated by condensation nor gravitational collision in the size range of 15–40 μm in radius. Turbulence-generated collision has been thought to be the mechanism to bridge the size gap, i.e., the bottleneck problem. This study develops the numerical approaches to study droplet growth in atmospheric turbulence and investigates the turbulence effect on cloud droplet growth. The collision process of inertial particles in turbulence is strongly nonlinear, which motivates the study of two distinct numerical schemes. An Eulerian-based numerical formulation for the Smoluchowski equation in multi-dimensions and a Monte Carlo-type Lagrangian scheme have been developed to study the combined collision and condensation processes. We first investigate the accuracy and reliability of the two schemes in a purely gravitational field and then in a straining flow. Discrepancies between different schemes are most strongly exposed when condensation and coagulation are studied separately, while their combined effects tend to result in smaller discrepancies. We find that for pure collision simulated by the Eulerian scheme, the mean particle radius slows down using finer mass bins, especially for collisions caused by different terminal velocities. For the case of Lagrangian scheme, it is independent of grid resolution at early times and weakly dependent at later times. Comparing the size spectra simulated by the two schemes, we find that the agreement is excellent at early times. For pure condensation, we find that the numerical solution of condensation by the Lagrangian model is consistent with the analytical solution in early times. The Lagrangian schemes are generally found to be superior over the Eulerian one in terms of computational performance. Moreover, the growth of cloud droplets in a turbulent environment is investigated as well. The agreement between the two schemes is excellent for both mean radius and size spectra, which gives us further insights into the accuracy of solving this strongly coupled nonlinear system. Turbulence broadens the size spectra of cloud droplets with increasing Reynolds number.

Sammanfattning

Molndroppstillväxt är ett av de mer utmanande problemen inom molnfysik. Speciellt tillväxten i intervallet $15 - 40\,\mu$m är en flaskhals eftersom varken kondensationsprocessen eller tillväxt genom kollisioner pga olika fallhastigheter är tillräckligt effektiv. En möjlighet som föreslagits är att tillväxten genom kollisioner kan ske hastigare i ett turbulent flöde. I denna studie utvecklas numeriska metoder för att studera dropptillväxt i atmosfärisk turbulens med avsikten att studera dess effekter påtillväxthastigheten. Kollisionsprocessen för partiklar som är påverkade av tröghetskrafter är mycket ickelinjär, därför testas tvåolika numeriska metoder. En multidimensionell Eulersk metod baserad påSmoluchowskiekvationen och ett Lagrangeskt schema av Monte Carlotyp är utvecklade för att samtidigt studera tillväxt genom kondensation och kollision. Noggrannheten och tillförlitligheten för de tvåschemana studeras först i förenklad form, enbart för kollisioner pga gravitationen eller för ett sk "straining flow". Skillnaden mellan metoderna är tydligast i experiment när kondensation och kollision studeras separat. För bara kollision med det Eulerska schemat sker tillväxten av medelradien långsammare när fler beräkningsintervall används för dropparnas massa; detta gäller speciellt för kollisioner som orsakas av dropparnas olika fallhastigheter. Det Lagrangeska schemat är däremot oberoende av upplösningen av beräkningsgriddet tidigt i experimenten för att sedan ha ett begränsat inflytande. De simulerade storleksfördelningarna för båda metoderna stämmer mycket väl överens i början av simuleringen. Resultaten för den Lagrangeska metoden, vid enbart kondensation, ger samma resultat som en analytisk lösning i början av simuleringen. Det Lagrangeska schemat är generellt bättre än det Eulerska avseende beräkningstiden. Eftersom de tvåmetoderna ger lika resultat med avseende påbåde medelradie och storleksfördelning, kan numeriska experiment ge oss större förståelse för detta ickelinjära system. Preliminära resultat visar att turbulensen breddar storleksfördelningen av molndroppar samt att breddningen ökar med ökande Reynolds tal.

Paper included in the thesis

PAPER I: **Eulerian and modified Lagrangian approaches to multi-dimensional condensation and coagulation**
Xiang-Yu Li, A. Brandenburg, N. E. L. Haugen, and G. Svensson
J. Comp. Phys., submitted, arXiv:1604.08169, 2016.

Author's contribution

We started the project from scratch. I am one of the core members of the project and actively involved in all the discussions, developments, and simulations, having designed most of them either by myself or in consultation with my coauthors. I wrote many parts of the text and suggested changes of the other parts written by my coauthors. I performed all the simulations and produced most of the plots.

Contents

1. Introduction

Clouds, the regulator of the radiative heating of the planet [1], represent a major complication in the current representations of the climate system [2]. The albedo of clouds largely depends on the spatial distribution and the size of cloud droplets [3]. Experimental studies have allowed detailed insights about the size distributions of droplets [4]. Turbulence has been considered to play a crucial role in the spatial distribution [5] and the growth of cloud droplets [6]. Therefore it is of fundamental importance to investigate the cloud droplets growth in the turbulent environment. In this study, we will mainly focus on the bottleneck problem of cloud droplet growth [7], one of the main challenges for cloud physics. The bottleneck problem states that the size range of approximately 15–40 μm[1], in which neither condensational growth nor collisional growth due to gravity dominate the increase of the droplet size [7].

The growth of cloud droplets is dominated by two processes: condensation and collision [8]. Condensation dominates the growth between the size range of 2–15 μm [8] and the droplet radius growth rate is inversely proportional to the radius, implying that a larger droplet grows slower than a smaller one, which generates a narrow size distribution [7]. Thus, droplet growth by collision is required to complete the growth mechanism for the formation of the rain droplet. Collisions between droplets happen when their mutual velocities are directed toward each other. In the absence of turbulence, this can happen when droplets have different sizes such that their terminal fall velocities are different. Gravitational collision plays a significant role in droplet growth within the size range of 50–100 μm [7, 8]. However, it cannot explain the size gap of the growth, therefore turbulence-generated collision has been proposed to explain the bottleneck problem.

Previous studies suggested that turbulence acceleration is mainly due to the turbulence enhancement effect on collision probability [5, 7, 8]. As far back as 1939, Arenberg recognized qualitatively that turbulence can enhance the collision rate and relative motion of cloud droplets [9], followed by semi-analytical studies of Gabilly [10] in 1949 and East & Marshall [11] in 1954. In 1956, Saffman & Turner developed a theoretical model for the turbulence enhancement effect on relative motion of weak-inertia cloud droplets [12]. The stochastic model was first introduced in 1988 by Reuter [13], suggesting that turbulence could enhance the gravitational kernel. In recent years, by adopting the concept of radial distribution function, several works have shown that

---

[1] In present context, size is in radius instead of diameter.

turbulence can accelerate the rain formation through increasing the collision efficiency and radial relative velocity [7, 14, 15]. Wang & Grabowski studied the turbulence effect on warm rain development by comparing the turbulence kernel with the gravitational kernel, concluding that the turbulence enhancement factor is about 2 [14].

Turbulence could also affect the condensation process by changing the distribution of supersaturation. Vaillancourt investigated the turbulence effect on the condensation process by direct numerical simulation (DNS[1]) and argued that small-scale turbulence has negligible effect on the condensation process owing to rapid rearrangement of droplet positions [16]. However, Lanotte et al. conducted similar DNS and found the width of the cloud droplet radius increases with increasing Reynolds number [17], which is further confirmed by Sardina et al. [18].

In the astrophysical context, the size gap problem of planetesimals via meter-sized accretion is still a puzzling process [19]. The planetesimals, the kilometer-sized planetary precursors, are formed from micrometer-sized protoplanetary dust particles. In this growth process, both condensation and coagulation are involved in. Particles with size smaller than millimeter grow by sticking together owe to contact forces. Kilometer-sized and even larger bodies coagulate by gravity-generated and turbulence-generated collision. However, the turbulence-generated collision is a barrier to study the planet formation. Particles grow from millimeter to kilometer-sized planetesimals by condensation process, which is a conclusion rely on several assumptions and simplifications [20]. The formation of planetesimals involves not only collision and condensation process, but also fragmentation and bounce. Moreover, these processes are entangled with turbulence, therefore the combination of collision, fragmentation processes and turbulence renders the growth process a strongly nonlinear problem. Thus further study is required to bridge the size gap for planet formation in astrophysical context and cloud-droplet formation in meteorological context.

To have a comprehensive understanding of the turbulence effect on cloud droplet formation, here we combine the condensation and collision process to simulate the entire growth process of cloud droplets by DNS. We solve the Smoluchowski equation combined with the condensation equation in a weakly compressible turbulent gas flow in an Eulerian framework using the PENCIL CODE [21]. Moreover, since the collision process of inertial particles in turbulence is strongly nonlinear, the Lagrangian scheme is employed to compare with the Eulerian one. The Lagrangian scheme is technically more compli-

---

[1] DNS is the numerical method of solving the nonlinear physical equations directly without adopting any sub-grid models, and thus to resolve the dissipation scale of turbulence.

cated than the Eulerian one, but it provides a more physical representation of the dynamics properties of cloud droplets. In the current context we adopt the modified-Lagrangian approach to simulate the collision process of cloud droplets with huge number density (at least $n_0 = 10^8\,\mathrm{m}^{-3}$). We refer to the modified-Lagrangian scheme here as swarm model. The advantages of the swarm model are two-fold. On the one hand, it tracks the individual cloud droplets along their trajectories, which also means that artificial viscosities used in the Eulerian scheme to stabilize the simulation can be avoided. On the other hand, it allows cloud droplets in large domains to be treated in a stochastic manner.

The observation of the cloud droplet number concentration (CDNC) can help verify the numerical simulations. The liquid water content (LWC) within clouds is determined by the spatial distribution and size of cloud droplets. Therefore it is important to measure these two quantities in the cloud. Leaitch et al. [22] measured the size spectra and liquid water content (LWC) of stratiform clouds and cumululiform clouds respectively using aircrafts since 1982. Their measurement shows that the CDNC is $n \approx 20-150\,\mathrm{cm}^{-3}$ in cumululiform clouds and $n \approx 170-370\,\mathrm{cm}^{-3}$ in stratiform clouds respectively. In 1993, Martin et al. [23] presented the experiments of warm stratocumulus clouds in the eastern Pacific, South Atlantic, subtropical regions of the North Atlantic, and the sea areas around the British Isles. They found that the shape of the size spectra strongly depends on the properties of cloud condensation nuclei (CCN). Since then many observational experiments have observed CCN, CDNC and turbulence in marine stratocumulus e.g. BOMEX, ATEX [24], and DYCOMS [25]. Recent observations focus more on the entrainment. Small et al. [26] analyzed the measured CDNC and LWC from the Artium Flight phase-Doppler interferometer and found the mixing in clouds is inhomogeneous, which is further confirmed by more accurate measurement by Beals et al. [3]. Nevertheless the mechanism of inhomogeneous mixing is still unclear, which may require more investigation.

2. Growth of cloud droplets in a turbulent environment

2.1 Condensational growth

When a cloud droplet is exposed in a supersaturated environment, it will grow due to the net water vapor flux towards the surface, resulting in the condensational growth law

$$r\frac{\mathrm{d}r}{\mathrm{d}t} = GS, \tag{2.1}$$

where G is a coefficient that is weakly dependent on temperature and pressure, and S is the supersaturation ratio. The condensational growth law results in slow growth of cloud droplets, $r \sim t^{1/2}$, which is similar to Einstein's theory of Brownian motion and the single-particle dispersion law in turbulence [27]. As can be seen from Equation (2.1), the growth rate of cloud droplets is inversely proportional to the radius, suggesting that larger cloud droplets grow slower than smaller ones. This will narrow the size spectra of cloud droplets under the assumption that the supersaturation ratio is positive and uniform. Supersaturation, as the driver of condensational growth, however is spatially inhomogeneous. The basic parcel model in the Meteorological context suggests that the supersaturation is proportional to the updraft velocity and inversely proportional to the mean radius and number density of cloud droplets [8]. The flow within the cloud is highly turbulent, thus one may expect that turbulence can contribute to the spatial distribution of supersaturation and therefore affect the size spectra of cloud droplets even though the size of cloud droplets is much smaller than the Kolmogorov length scale ($\approx 1\,\mathrm{mm}$) of the cloud turbulence. In fact, turbulence also has an effect on the local temperature field and therefore the vapor mixing ratio [28]. The supersaturation can then be determined by Equation (5.1) discussed in Section 5.2. Lanotte [17] and Sardina [18] found that the width of the size spectra of cloud droplets increases with increasing Reynolds number [17]. Assumptions in these studies limit the variations of the supersaturation since thermodynamics is neglected and the supersaturation is solely transported by turbulence with zero mean velocity and supersaturation ratio. In addition, inhomogeneous mixing of dry air and vapor at the cloud edge, or entrainment, is not accounted for and observations [3] show that this plays an important role for the evolution of supersaturation. The entrainment is not emphasized in the present study, but it will be a subject of future studies. It is worth noting that an adequate investigation of the condensational growth depends on the appropriate representation of supersaturation. The modelling of supersaturation requires the combination between micro-scale and macro-scale dynamics as well as the coupling of turbulence and thermodynamics. Condensational growth law in the astrophysical context is similar to that in the meteorological context [20] in the sense that the growth of particles is due to the vapor flux towards the surface.

2.2 Collisional growth

Cloud droplets grow from $2\,\mu$m to $500\,\mu$m to become raindrops. Condensation plays a very important role in the size range of $2\,\mu$m–$20\,\mu$m. But, as discussed above, it leads to narrow size spectra of the cloud droplets. Therefore, another efficient mechanism is required to drive the growth, i.e. the collision process.

2.2.1 Continuous collision from different terminal fall velocities

The most basic mechanism causing collisions among cloud droplets is the gravity-generated collision. Considering the following continuous collision process that one large cloud droplet with radius r_L (corresponding to terminal velocity v_L) collide with a smaller one with radius r_S, (corresponding to terminal velocity v_S) the mass growth rate of the larger one can be expressed as [8]

$$\frac{\mathrm{d}m_d}{\mathrm{d}t} = K(r_L, r_S) w_l, \tag{2.2}$$

where

$$K(r_L, r_S) = \pi (r_L + r_S)^2 |v_L - v_S| E \tag{2.3}$$

is the collision kernel and w_l is the liquid water concentration. The collision kernel is defined as the volume swept out per unit time per density in the collision process [29]. E is the collision efficiency tabulated by Hall [30]. In the present study, the collision is assumed to be perfect and E is unit for simplicity. When the collector is much larger than the collected cloud droplet in size, the collision kernel can be simplified as $K(r_L, r_S) = \pi r_L^2 |v_L|$. In the size range of $100\,\mu$m–$500\,\mu$m, the descent speed of the cloud droplet is roughly proportional to its size if the droplet remains spherical, i.e. $|v_L| \sim D r_L$, where $D \approx 4000\,\mathrm{s}^{-1}$ [8]. Thus, the mass growth rate of the collector can be approximated as $\mathrm{d}m_d/\mathrm{d}t \approx \pi D r_L^3 w_l$, giving an exponential growth behavior.

2.2.2 Stochastic collision through turbulence

The continuous collision will become effective only if there are large enough collectors. To start the process, a triggering collector is needed which is some-times referred to as the "lucky" cloud droplet. Where does the lucky one come from? The "lucky" cloud droplet is assumed to emerge from the stochastic collision process. As discussed in Section 2.2.1, gravity plays an important role for the continuous collision, which is however not the case for stochastic collisions, since gravity cannot dominate the motion of cloud droplets with sizes in the range of 2–50 μm. We recall that the Reynolds number of turbulent flow within clouds is $\mathrm{Re} \approx 10^7$; thus turbulence likely contributes to the stochastic collision process. The total number density of cloud droplets is about $10^8\,\mathrm{m}^{-3}$, indicating that 3×10^8 freedom has to be solved by numerical simulation if each individual cloud droplet is tracked. Therefore, stochastic method is necessary to solve the collision problem. To characterize the spatial distribution and time evolution of cloud droplets, the number density distribution function $f(\boldsymbol{x}, r, t)$ is adopted. The main aim in the present thesis is to determine $f(\boldsymbol{x}, r, t)$ in a turbulent environment by DNS.

When two cloud droplets collide with each other, they may coalesce, rebound and disrupt. In the present study, we consider perfect collision and neglect the fragmentation. Here we limit the discussion to fragmentation and disruption. The disruption of cloud droplets redistributes water mass into smaller ones, which on the one hand can slow down the growth of cloud droplets, but on the other hand, it can broaden the size spectra of cloud droplets. Studying the disruption in the growth process may become another subject of future studies [8]. Fragmentation is also important for the understanding of planet formation in the sense that it is the key issue of the meter-size barrier for the planet formation. The problem of the meter-size barrier states that particles obtain large relative velocity when they reach a size of decimeters to meters so that collisions at large relative speeds lead to fragmentation and bounce instead of coagulation. Thus, the growth of particles in this size range stalls. There have been several works trying to explain the meter-size barrier, but an appropriate representation of the kernel is required to overcome the growth obstacle [31].

3. Numerical models

In this thesis, two stochastic methods that allow for fluctuations are employed. The Smoluchowski model and a modified-Lagrangian (superparticle) model. We refer to the Smoluchowski model as Eulerian model and to the modified-Lagrangian model as swarm model; see details about the two models in Paper I.

3.1 Eulerian model

The Eulerian model is widely used in both meteorological [8, 12, 32] and astrophysical [31] contexts to simulate the collision process. The spatial distribution of cloud droplets varies dramatically because of collisions and entrainment. For a given number density of cloud droplets with different size, the collision process yields an increasing number of larger cloud droplets and a decreasing number of smaller ones. Thus the rate of change of the number density can be expressed by the gain of larger cloud droplets and the loss of smaller ones, which is referred to as the Smoluchowski equation. The Smoluchowski equation is a nonlinear equation, when coupled with the hydrodynamic equation of the air flow and the momentum equation of cloud droplets, it becomes even more complicated. For the kernels of the form (2.3), there are no analytical solution so far. Therefore, DNS are adopted to investigate the growth of cloud droplets.

3.2 Swarm model

Compared with the Eulerian model, Lagrangian modelling of the collision of inertial particles is closer to the nature of real physical collisions in that it takes fluctuations automatically into account. However, the Lagrangian tracking has the following drawbacks. First, it is limited by the physical size of the system [33]. The typical mean number density of cloud droplets in stratocumulus cloud is $n = 10^8\,\mathrm{m}^{-3}$. Assuming that the maximum number that we can handle on a supercomputer is $N_p = 10^8$, the largest computational domain we can simulate has a volume of $N_p/n = 1\,\mathrm{m}^3$ This value is much less than the volume corresponding to the typical turbulent integral length scale of clouds of about $100\,\mathrm{m}$. Second, it is numerically expensive and difficult to implement the collision process in the sense that the potential collision partners in neighboring grid cells have to be considered. Considering the above restrictions of the direct Lagrangian approach, we employ Monte Carlo-type Lagrangian tracking to model collisions between numerical super-particles, which is a statistical approach to represent swarms of physical particles [34]. We refer to this statistical Lagrangian model as the swarm model. The swarm model is also referred to as the super-particle or super-droplet model [35]. The essence of the Monte Carlo method is to track the super-particles consisting of physical particles instead of tracking the individual physical particles. The behavior of super-particles is assumed to be a good representation of all physical particles. A collision will only happen if two swarms reside in the same grid cell. Therefore, it is technically much easier to implement the collision processes and numerically inexpensive compared with the direct Lagrangian approach. We also assume that the collision only happens among one super-particle and physical particles that do not belong to the super-particle. This requires that the number of superparticles is much smaller than the number of physical particles. More importantly, the swarm model allows us to deal with large domain sizes (see Paper I for details). Therefore the swarm model allows us to follow collisions together with hydrodynamics in a large domain at a moderate computational cost [33].

4. Results

4.1 Eulerian model

4.1.1 Sensitivity to parameters

To investigate the sensitivity to changes in the parameters, zero-dimensional (0-D) simulations of gravity-driven collision, condensation, and combined processes are conducted with varying parameters.

Mass bin resolution dependency

In this section, we discuss the numerical convergence of the Smoluchowski equation solved using the mass bin method. To address the MBR dependency, it is convenient to define the mean radius $\bar{r}$ and the total number density distribution n from $f(\boldsymbol{x},r,t)$. The $\bar{r}$ is given by

$$\bar{r} = \int_0^\infty f(\boldsymbol{x},r,t) r \,\mathrm{d}r \Big/ \int_0^\infty f(\boldsymbol{x},r,t) \,\mathrm{d}r, \tag{4.1}$$

and n is given by

$$n(\boldsymbol{x},t) = \int_0^\infty f(\boldsymbol{x},r,t) \,\mathrm{d}r. \tag{4.2}$$

First, we investigate the MBR dependence of the condensation process. The upper panel of Figure 4.1 shows that the evolution of the mean radius is weakly MBR dependent using an isotropic supersaturation. However, as shown in the lower panel of Figure 4.1, its size spectra strongly depend on MBR in the sense that the numerical solution cannot match the analytical solution even with $k_{\max} = 1281$. The coagulation process exhibits strong MBR dependency, as shown in the left panel of Figure 4.2, where $\bar{r}$ is seen to diverge even at the highest mass bin $k_{\max} = 3457$. Such a large MBR is impractical for DNS. Thus, we will focus more on the Lagrangian method in future studies. Nevertheless, the combined condensational and collisional growth weakly depends on MBR when $k_{\max} \geq 55$ as shown in Figure 4.2. This is due to the fact that the condensation process narrows the size spectra, resulting in very narrow size spectra for the coagulation process. Meanwhile, the coagulation process is dramatically more efficient than the condensation process. Therefore, the evolution of $\bar{r}$ converges rapidly when both condensation and coagulation processes are involved. We therefore conclude that it is advantageous to adopt the Lagrangian scheme to model the condensation and coagulation processes.

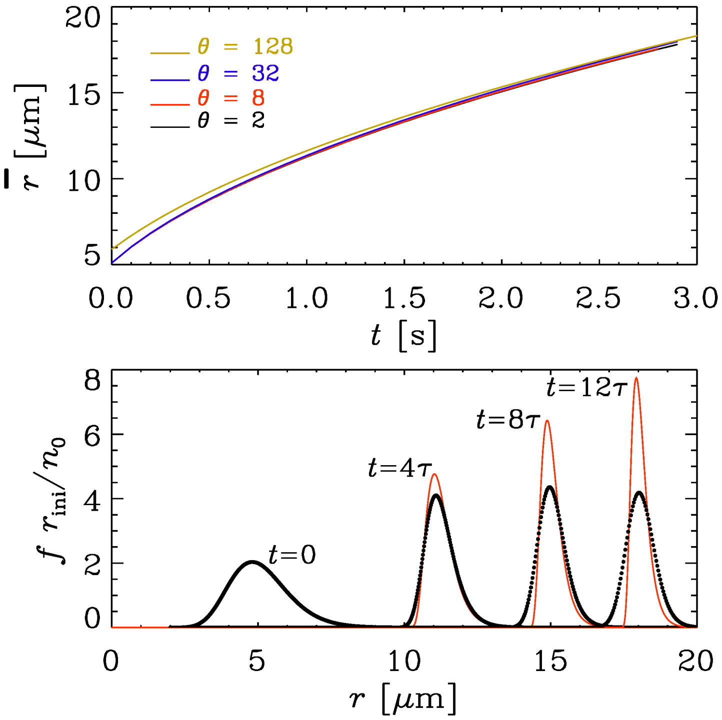

Figure 4.1: Evolution of mean radius with different MBR in the case of pure condensation simulated by Eulerian model (upper panel). The supersaturation value is given as $S = 0.01$. The parameters of the initial distribution are $\sigma = 0.2$, $r_{\text{ini}} = 5\,\mu\text{m}$ and $n_0 = 10^{10}\,\text{m}^{-3}$. The lower panel shows the size spectra of the case with $k_{\text{max}} = 1281$. The red curve in the lower panel is the analytical solution (See Equation (40) of Paper I) of condensational growth with constant supersaturation. Here, τ stands for the condensation time $\tau_{\text{cond}} = r_{\text{ini}}^2/2GS$.

Initial width dependency

In the present study, we adopt a lognormal function as initial distribution of cloud droplets. The lognormal function is widely used in atmospheric applications due to the fact that it is semi-empirical in nature and fits well with the observed distribution of aerosols and cloud droplets [36]. For numerical studies, it is necessary to prescribe the width σ, initial radius r_{ini} and the lower boundary of radius r_1 of the initial distribution given by Equation (29) of Paper I so that the simulation is independent of initial parameters, or at least only weakly depends on them. The upper panel of Figure 4.3 shows the evolution of the mean radius for two different initial widths, where the evolution is driven by collision only. The two radii are the same initially, but the one with

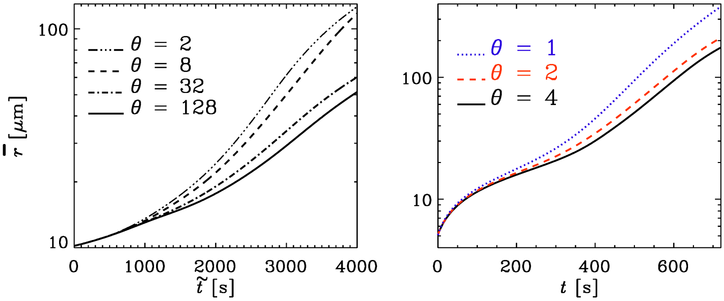

Figure 4.2: Evolution of mean radius with different MBR in the case of pure collision (left panel) as well as the one with both collision and condensation (right panel) simulated by Eulerian model. The parameters of the initial distribution for pure collision case are $\sigma = 0.2$, $r_{\mathrm{ini}} = 10\,\mu\mathrm{m}$ and $n_0 = 10^{10}\,\mathrm{m}^{-3}$; those for both collision and condensation are $\sigma = 0.2$, $r_{\mathrm{ini}} = 5\,\mu\mathrm{m}$ and $n_0 = 10^{8}\,\mathrm{m}^{-3}$. Here, $\tilde{t} = tn/n_0$. θ is chosen to be a power of two and defined such that $m_k = m_1\delta^{k-1}$ and $\delta = 2^{1/\theta}$, where m_k is the mass bins and m_1 is the initial mass bin.

wider distribution grows faster because the high-mass tail of the distribution matters, which is due to the fact that collision can only be triggered by certain large cloud droplets. However, when condensation is also turned on, the evolution becomes almost independent of width, as shown in the lower panel of Figure 4.3. This is because the condensation process shrinks the number density distribution. Other numerical issues, like the initial radius and lower boundary of radius, are studied as well. First, to investigate the sensitivity to the choice of the initial radius, 0-D simulations with different initial radii are carried out at a fixed low boundary of radius. Figure 4.4 shows that, as long as the initial radius r_{ini} is less than $10\,\mu$m, the subsequent evolutions of $\bar{r}$ and $m_{\mathrm{drop}}/m_{\mathrm{air}}$ are virtually identical, suggesting that the current numerical simulation to solve the Smoluchowski equation can be applied to the collision and coagulation problem with different initial sizes. Second, motivated by the fact that the simulation is independent of initial radius, the dependency on the lower boundary radius is also investigated. In most of the experiments, a lower boundary $r_1 = 2\,\mu$m is used, but, as shown in Figure 4.4, r_1 can be increased to $4\,\mu$m without any loss of accuracy, and even $r_1 = 8\,\mu$m is found to be accurate enough. The supersaturation value of maritime cloud in the atmosphere is $S \approx 0.01$. In Figure 4.5 we compare the evolution of the mean radius $\bar{r}$ and the mass ratio of liquid water to gas ratio, $m_{\mathrm{drop}}/m_{\mathrm{air}}$, for $S = 1.0$, 0.1, and 0.01 and $\sigma = 0.1, 0.2$, and 0.5. It is plausible that the evolution of the mean radius is independent of σ for $\sigma \leq 0.2$ with $S = 0.01$, but for $\sigma = 0.5$ the evolution depends on supersaturation. This is because the width $\sigma = 0.5$ is so large that for

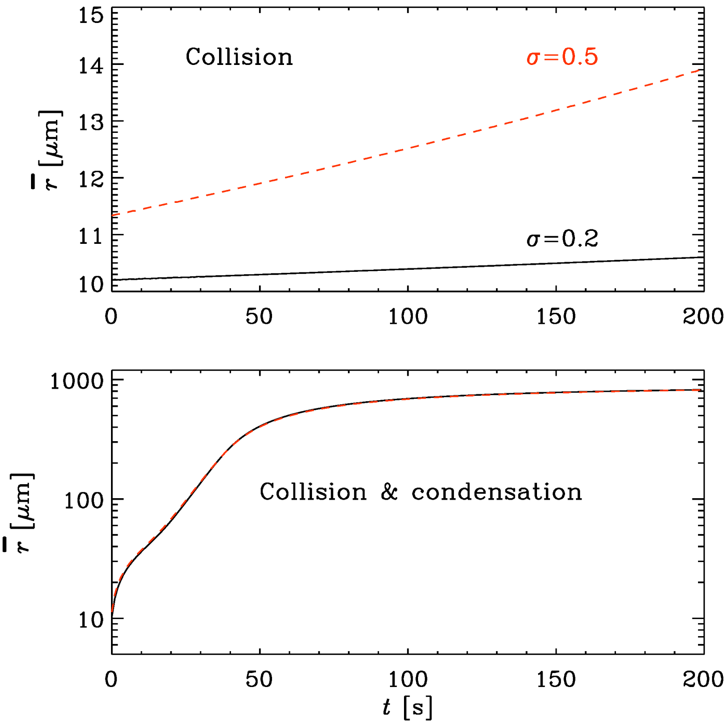

Figure 4.3: Evolution of mean radius for two different widths of the initial distribution (red line: $\sigma = 0.5$, black line: $\sigma = 0.2$). The upper panel represents the collisional growth of cloud droplets driven by gravity. The lower panel represents the combined collisional and condensational growth. The supersaturation value is given as $S = 1.0$. The parameters of the initial distribution are $n_0 = 10^8\,\mathrm{m}^{-3}$, $r_{\mathrm{ini}} = 10\,\mu\mathrm{m}$ and $r_1 = 2\,\mu\mathrm{m}$. The MBR is $k_{\mathrm{max}} = 55$.

the slow condensation with $S = 0.01$, collision can act on the largest droplets of the tail of the distribution, resulting in a different growth rate.

In summary, based on the tests discussed above, $k_{\mathrm{max}} \approx 55$, $\sigma \leq 0.2$, $S = 0.01$, $r_{\mathrm{ini}} \leq 14\ \mu\mathrm{m}$, $r_1 \leq 8\,\mu\mathrm{m}$, and $n_0 = 10^8\ \mathrm{m}^{-3}$ are chosen to simulate the two-dimensional (2-D) and three-dimensional (3-D) cases.

4.1.2 Comparison between Eulerian and swarm models

Although the Eulerian model is numerically expensive, it is still of value to solve and compare with the Lagrangian model to evaluate the accuracy and reliability of the solution of this strongly nonlinear system. In this section, we will summarize the main conclusions of the comparison between the Eulerian and Lagrangian schemes. We refer to Paper I for a detailed comparison.

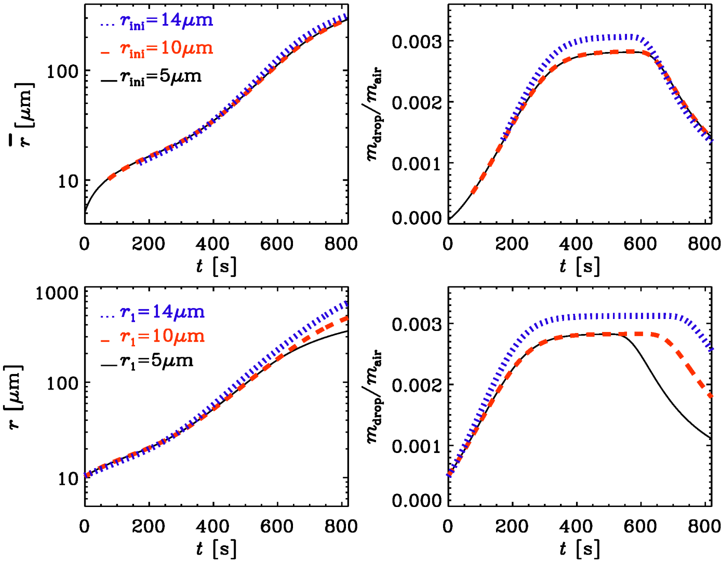

Figure 4.4: Dependence on r_{ini} (upper panels) for $r_{\mathrm{ini}} = 5\,\mu$m (black). $10\,\mu$m (red) and $14\,\mu$m (blue) using 55 mass bins, $\sigma = 0.2$ with condensation and collision at $S = 1\%$, $n_0 = 10^8\,\mathrm{m}^{-3}$. Dependence on r_1 (lower panels) for $r_1 = 2\,\mu$m (black), $4\,\mu$m (red) and $8\,\mu$m (blue).

Here, we limit the discussion to collision processes in a purely gravitational field or in a straining flow. The one in the turbulence case will be discussed in Section 4.2. The size spectra of condensational growth simulated by the Lagrangian model agree well with the analytical solution, while the one by the Eulerian model requires high MBR to match the analytical solution. For purely coagulational growth, the size spectra calculated from the two schemes agree well with each other at early times, but they depart at later times. The combined condensational and collisional process also shows agreement at early times, but deviates at late times. The evolution of the mean particle radius requires high MBR to converge in the case of the Eulerian scheme, but it is independent of spatial resolution at early times and weakly dependent at late times in the case of the Lagrangian scheme. We conclude that the Lagrangian scheme is superior over the Eulerian scheme regarding the convergence and the quality of statistics at given computational performance.

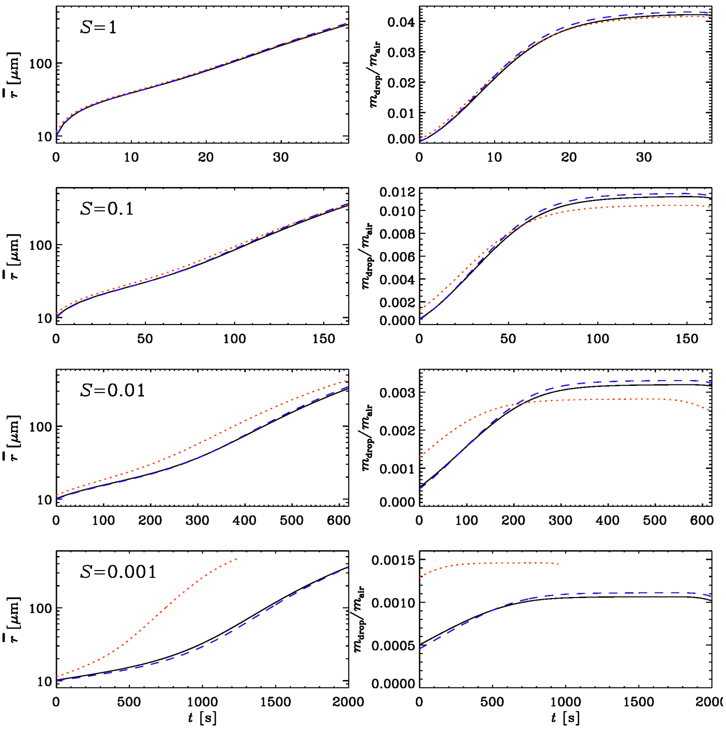

Figure 4.5: Evolution of mean radius with different supersaturation value in the case of combined condensation and collision simulated by Eulerian model. The parameters of the initial distribution are $\sigma = 0.2$, $r_{\text{ini}} = 5\,\mu\text{m}$ and $n_0 = 10^8\,\text{m}^{-3}$. The MBR is given as $k_{\text{max}} = 28$. The width of the initial distribution are given as $\sigma = 0.1$ (blue, dashed), 0.2 (back, solid) and 0.5 (red, dotted). It is interesting to note that the evolution is independent of σ for $\sigma \leq 0.2$.

4.2 Turbulence effect on cloud droplet growth

In this section, growth of cloud droplets in a turbulent environment using both swarm and Eulerian models will be explored. Air flow in the atmosphere is generally approximated by 2-D turbulence owing to its large aspect ratio [37] and high Reynolds number [38]. However, the dimension of atmospheric turbulence is strongly scale dependent. It is more physical to consider the dynamics of cloud droplets in 3-D turbulence rather than 2-D turbulence. Nevertheless, covering all the atmospheric scales in modern numerical simulations is challenging, which may be possible using quantum computers in the future. In the present study, we will adopt 2-D turbulence for the purpose of comparing the Eulerian model and the swarm model.

Our 2-D simulations are carried out in a domain with length $L = 0.5\,\text{m}$ and turbulence is driven by random forcing, resulting in the smallest wavenumber being $k_1 = 2\pi/L \approx 13\,\mathrm{m}^{-1}$. Energy is injected at $1/3$ ($k_\mathrm{f}/k_1 = 3$) of the box, leading to an average forcing wavenumber $k_\mathrm{f} \approx 40\,\mathrm{m}^{-1}$. The viscosity of the gas flow adopted in the current simulation is $\nu = 5 \times 10^{-4}\,\mathrm{m}^2/\mathrm{s}$. Thus, the Reynolds number can be obtained as[1] $\mathrm{Re} = u_\mathrm{rms} L_\mathrm{inj}/\nu = u_\mathrm{rms} L/(3\nu)$. The mesh-grid Reynolds number is defined as $\mathrm{Re}_\mathrm{mesh} = u_\mathrm{rms}\Delta x/\nu$, which should be less than[2] 5 in moderately compressive flows to ensure numerical stability of the simulation. In the present study, $\mathrm{Re}_\mathrm{mesh} \approx 2$. The Kolmogorov length scale is given by $\eta = \left(\nu^3/\varepsilon_K\right)^{(1/4)}$, where ε_K is the energy dissipation rate. The eddy turnover time is defined as $\tau_\mathrm{eddy} = L_\mathrm{inj}/u_\mathrm{rms}$.

Cloud droplets grow first by condensation and then, at larger radii, by collision. To simulate the comprehensive growth mechanism of cloud droplets, we solve both collision and condensation equations simultaneously. Even though the Reynolds number achieved in DNS is much smaller than that in the atmosphere, the enhancement effect on collision by turbulence is quite clear, as shown below.

The collision process is extremely complex. There is no analytical solution even with the most basic geometrical kernel. When the collision process is coupled with turbulence, it becomes even more complicated. To verify if the code is suitable to the turbulence case, one needs to solve the problem using at least two distinct approaches and compare the results; see details of the simulations in Table 4.1. As discussed in Paper I, it is advantageous to adopt the nearest grid point mapping (NGP) method for the swarm scheme. However, we here emphasize that it does not seem to be important for turbulence, as shown in the inset of Figure 4.6. Turbulence continues to mix particles all the time while the straining flow tends to sweep up particles into predetermined locations that do not change. Nevertheless we would strongly recommend to use NGP in the swarm scheme. We recall that the mean particle growth is strongly MBR dependency for gravity, and less strongly for the straining flow (see details in Paper I). As shown in the inset of Figure 4.6, it weakly depends on MBR in turbulence. Thus, we conclude that the MBR dependency is closely related to the temporal and spatial properties of the flow. After investigating the convergence statistics of Smoluchowski equation and the swarm model in turbulence, we first compare the evolution of the mean radius simulated by the two schemes. As shown in Figure 4.6, the values of $\bar{r}$ agree well with each other from 0–2,000 s for $\mathrm{Re} \approx 115$, after which they depart from each other, but follow the same trend. The result is similar for $\mathrm{Re} \approx 233$, but the time

---

[1] This is one way to define the Reynolds, another way is to defined as $\mathrm{Re} = u_\mathrm{rms}/\nu k_\mathrm{f}$, which is used in Paper I.

[2] This criterion depends on the nature of the flow. If there are no shocks in the gas, it can be larger than 5.

Table 4.1

Scheme	mesh	N_p	$\lvert f \rvert$ (N)	IM	Processes	$k_{\max}$	$u_{\rm rms}$ (m/s)	Re
Swarm	256	3×10^5	2×10^{-2}	CIC	Coa	–	0.36	115
Swarm	256	3×10^5	2×10^{-2}	CIC	Con & Coa	–	0.36	115
Swarm	256	3×10^5	2×10^{-2}	NGP	Coa	–	0.36	115
Swarm	512	1.2×10^6	4×10^{-2}	CIC	Coa	–	0.74	233
Swarm	512	1.2×10^6	4×10^{-2}	CIC	Con & Coa	–	0.74	233
Swarm	512	1.2×10^6	4×10^{-2}	NGP	Coa	–	0.74	233
Euler	256	–	2×10^{-2}	–	Coa	53	0.36	115
Euler	256	–	2×10^{-2}	–	Coa	109	0.36	115
Euler	256	–	2×10^{-2}	–	Coa	53	0.36	115
Euler	512	–	4×10^{-2}	–	Con & Coa	53	0.74	233
Euler	512	–	4×10^{-2}	–	Con & Coa	53	0.74	233

Simulations in 2-D turbulence with both swarm model and Eulerian model. The viscosity of the gas flow is $\nu = 5\times10^{-4}\,\mathrm{m^2\,s^{-1}}$ in the present simulations. For the Eulerian model we adopt artificial viscosity and enhanced Brownian diffusivity for the particles ($\nu_{\rm p} = D_{\rm p} = 10^{-3}\,\mathrm{m^2\,s^{-1}}$).

interval is only between 0–1,000 s. We recall that the collision process in a turbulent environment is strongly nonlinear. However, the agreement between the swarm model and the Eulerian model gives us a sense of the accuracy of the solution. Moreover, both approaches show a counterintuitive peak in the evolution of mean radius, which is plausible and will be discussed later.

One might have thought that the evolution of the mean radius would show the growth of cloud droplets most directly. However, the mean radius cannot display the details of the growth, thus the number density distribution function $f(\boldsymbol{x},r,t)$ is adopted to investigate the details of the growth. Moreover, $f(\boldsymbol{x},r,t)$ is the key to the problem, which gives us the spatial distribution of cloud droplets as functions of time, position, and size. Figure 4.8 shows a comparison of size spectra between the swarm model and the Euler model in the case of pure collision at Re $\approx$ 233. The agreement of the spectra is excellent within 3000 s and especially for smaller particles.

We emphasize here that the agreement of size spectra between the swarm model and the Eulerian model in turbulence can shed some light on exploring the collision process of inertial particles in a turbulent environment. Thus, we can use both schemes to investigate the Reynolds number effect on the growth of cloud droplets; see details of the simulations in Table 4.1. We first inspect the case with pure collisions driven by turbulence. Both swarm and Eulerian

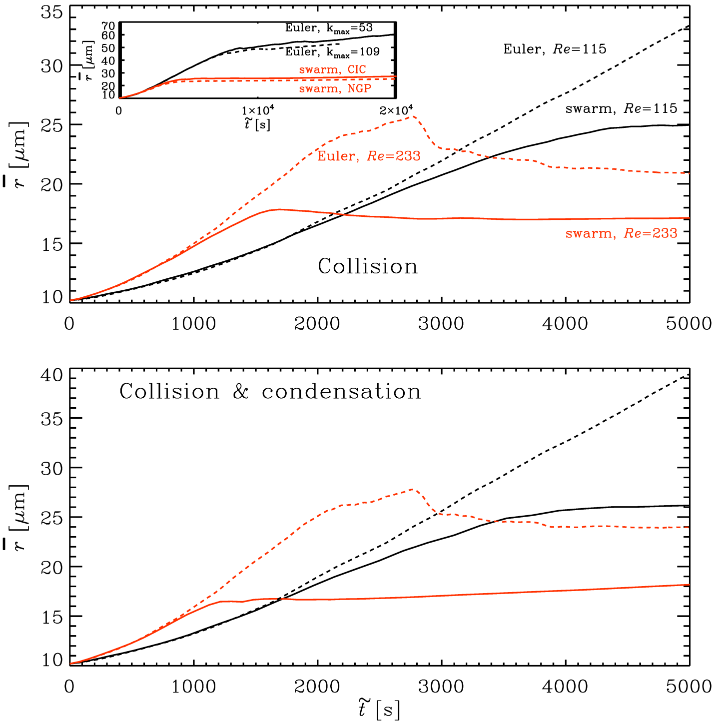

Figure 4.6: Comparison between 2-D swarm (approach II) model and the Eulerian model. The solid curves represent swarm model and the dashed ones represent Eulerian model. The upper panel represents the case with pure collision process, the lower one represents the case with both collision and condensation processes. The parameters of the initial distribution are given as $\sigma = 0.2$, $r_{\text{ini}} = 10\,\mu\text{m}$ and $n_0 = 10^{10}\,\text{m}^{-3}$. We refer to Table 4.1 for the details of the simulations. The inset shows the mean radius growth simulated by Eulerian model with $k_{\text{max}} = 53$ and $k_{\text{max}} = 109$, by swarm model with interpolation method CIC and NGP.

models illustrate that turbulence can broaden the size spectra with increasing Reynolds number, as shown in Figure 4.8, which can be intuitively illustrated by comparing the mean radius evolution in the upper panel of Figure 4.6. The broadening effect is crucially important to explain the "lucky cloud droplet" formation during the stochastic collision process. To our knowledge, it is the first time that the combined collision process of inertial particles, momentum of inertial particles and the turbulent gas flow are solved by DNS without adopting any types of subgrid scale models. This work provides a detailed study of the turbulence enhancement effect on raindrop formation. Further detailed studies of the enhancement mechanism need to be conducted, however.

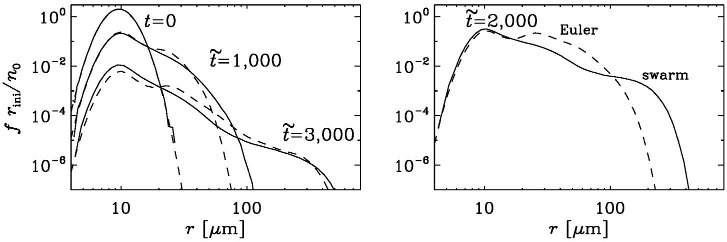

Figure 4.7: Comparison of the size spectra between the Eulerian model and the swarm model in the case of pure collision. The Reynolds number here is Re $\approx$ 233, corresponding to the red curves in the upper panel of Figure 4.6. The solid lines represent the result simulated using the swarm model and the dashed lines represent the one by the Eulerian model.

The combined condensational and collisional growth in turbulence is also investigated. It shows the same behavior as the case with pure collision. This is, on the one hand, due to the fact that condensation is here simulated using isotropic supersaturation, while on the other hand, the collision process dominates the growth of cloud droplets in the size range of 20–100 μm. To model the condensation process more realistically, one needs to solve the coupled physics of thermodynamics and turbulence, which will be discussed in Section 5.2.

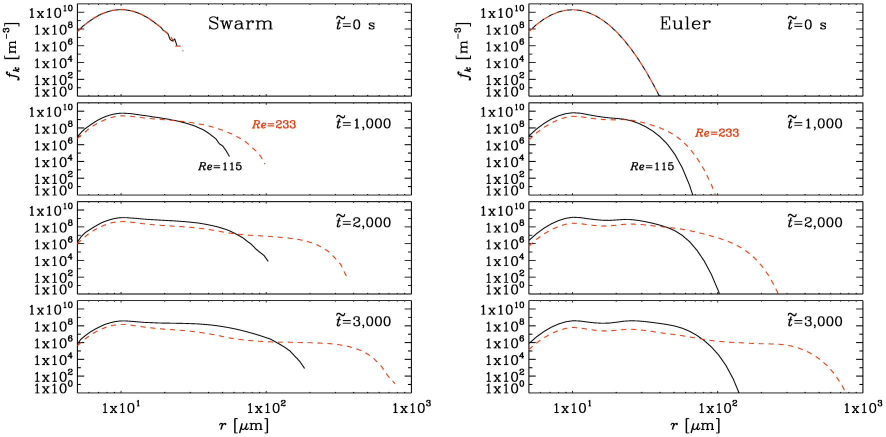

Figure 4.8: Size spectra for Re $\approx$ 155 and Re $\approx$ 233, corresponding to the upper panel of Figure 4.6.

4.3 The counterintuitive "peak"

Figure 4.6 shows the counterintuitive, but, natural peak. In this section, we will explore the cause of the "peak". For the following discussion, it is convenient to introduce the moments of the size spectra

$$M_\zeta = \sum f(r)\, r^\zeta. \tag{4.3}$$

so that $\overline{r} = M_1/M_0$. We emphasize here that the mean radius is determined by both the instantaneous size spectra and the radius. When two very small particles coalesce, the sum of all radii does basically not change, but the number of particles decreases by one, so the average increases. By contrast, when two large particles coalesce, the particle number again decreases by one, but the sum of the radii decreases from 2 to $2^{1/3} \approx 1.26$ due to the mass conservation assumption during the collision process, so the average also decreases, as shown in Figure 4.9. Thus, when the peak appears, it means that larger particles coalesce. We refer to Appendix B of Paper I for a detailed mathematical explanation of the peak.

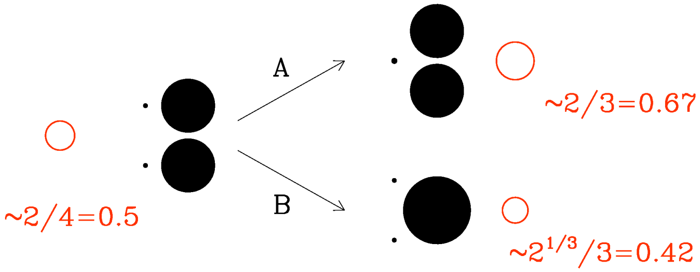

Figure 4.9: Sketch illustrating the growth of $\overline{r}$ when two small particles coalesce (A) and the decrease of $\overline{r}$ when two large particles coalesce (B). Filled black symbols denote actual particle sizes and open red symbols and red text refer to $\overline{r}$.

It is worth noting that the evolution of the mean radius driven by gravity-generated collision does not show the bump. This motivates us to explore the physics behind it. The spatial variation of $f(\boldsymbol{x}, r, t)$ in the case with gravity is much weaker than in the case with turbulence.

In a turbulent flow, one would expect that the clustering caused by turbulence will contribute to the size redistribution rate $(\partial M_1/\partial t)$ and the dilute rate $(\partial M_0/\partial t)$. The issue of whether clustering of cloud droplets enhances the collision rate is still debated. However it is generally suggested that the clustering or the preferential concentration contributes to the collision rate of cloud droplets. The Reynolds number dependency and Stokes number dependency of clustering have been intensively studied from 1956 [39] up to now. Here the Stokes number (St) characterizes the inertial effect of massive particles in a flow. The average Stokes number is in the range of 10^{-4}–10^{-2} in clouds [40], which is smaller than the triggering value $\mathrm{St} > 0.1$ that can make the droplet feel the effect of clustering [41]. However, the analysis of the observational data by Shaw [42] reveals droplet clustering even in cumulus clouds, which are free of entrained ambient air. Dallas [40] adopted the same analysis with Saffman [39] but using the local Stokes number to characterize the clustering, which demonstrates that turbulence can initiate and sustain a rapid growth of very small water droplets because of the extremely broad range of local Stokes numbers of identical droplets in the turbulence flow. Collins [43] found that the degree of preferential concentration increases with increasing Reynolds number. Later on, he concluded that the radial distribution function approaches a plateau with increasing Reynolds number [41]. However, Perrin et al. [44] found by means of DNS in isotropic cloud-like turbulence that droplets do not collide where they preferentially concentrate but in regions with significantly higher dissipation rates. Subsequently, Perrin et al. [45] conducted DNS to study the distribution of relative velocities between particles and found excellent agreement with the theoretical model of Gustavsson and Mehlig [46]. They argued that the distribution of the relative velocity of particles exhibits the same universal power-law in the case that the relative motion of particles is dominated by caustics. The observation by Beals et al. [3] shows that turbulent mixing within clouds is extremely inhomogeneous, indicating that the clustering contributes to the spatial distribution of cloud droplets, although they do not necessarily enhance the growth of cloud droplets. Therefore, further study is needed to address this issue conclusively.

In the present study, we only show that clustering occurs in the collision process and can affect the spatial distribution of cloud droplets. We do not claim that clustering contributes to the collision rate. The common understanding of the clustering of finite-size inertial particles relies on the idea that vortices act as centrifuges ejecting particles heavier than the fluid and trapping lighter ones [47] below the Kolmogorov length scale in a turbulent flow. As shown in Figure 4.11, this is the case in our present study. Turbulence enhances the clustering of cloud droplets, thus resulting in a rapid increase of the dilute rate. When the dilute rate becomes larger than the size redistribution rate, the evolution of the mean radius of cloud droplets will decrease. It is interesting to define the collision time scale and the clustering time scale. Then, the effect of clustering on the collision rate can be quantitatively determined. To characterize particle clusters at scales below the Kolmogorov length scale, and thus the clustering time scale, the correlation dimension D_2 can be measured.

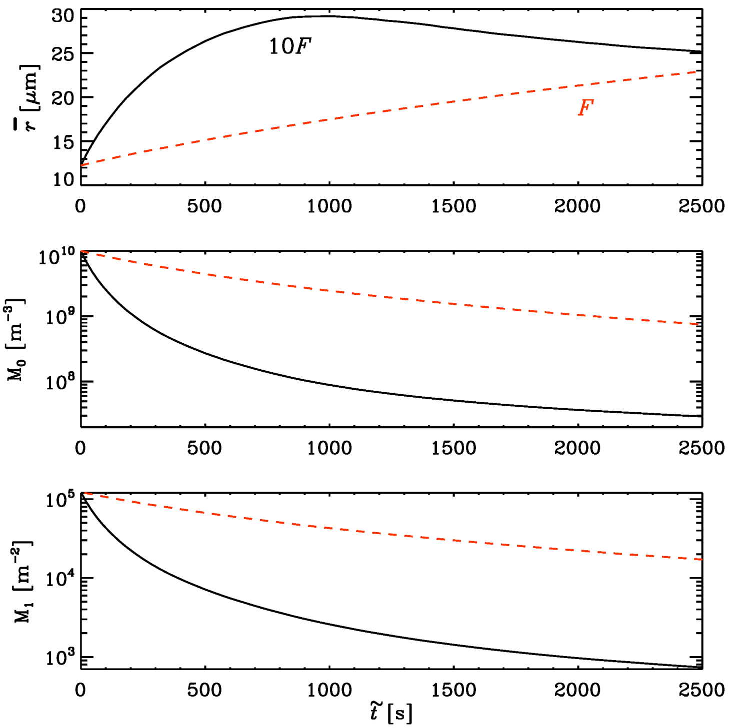

Figure 4.10: Evolution of the mean radius, zeroth moment and the third moment in a kinematic straining flow. The combined collision and condensational growth is simulated by 3-D swarm (Scheme II) model. The parameters of the initial distribution of size spectra are $r_{\mathrm{ini}} = 12\,\mu$m, $n_0 = 10^{10}\,\mathrm{m}^{-3}$ and $\sigma = 0.2$. The parameters for the condensation are given as $G = 10^{-11}\,\mathrm{m}^2/\,\mathrm{s}$ and $S = 0.01$. Here, F represents the amplitude of the straining flow in m/s.

It is estimated through the small-scale algebraic behavior of the probability to find two particles at a distance less than a given d: $P_2(d) \sim d^{D_2}$. If the spatial distribution of inertial particles is homogeneous, D_2 is the largest. Conversely, the minimum D_2 corresponds to the maximum clustering [48]. Bec et al. [48] found that D_2 depends weakly on Re_λ. For all values of Re_λ, a maximum of clustering is observed for $S_\eta \approx 0.6$. Calculating D_2 with variable Stokes number is challenging in our present work, which is still in progress.

Turbulence leads to clustering of cloud droplets, thus resulting in an extremely inhomogeneous spatial distribution of cloud droplets. To verify our explanation of the peak of mean radius, we study the growth of cloud droplets in a less chaotic flow, the divergence-free kinematic straining flow. We investigate the combined isotropic condensation with collision simulated by the

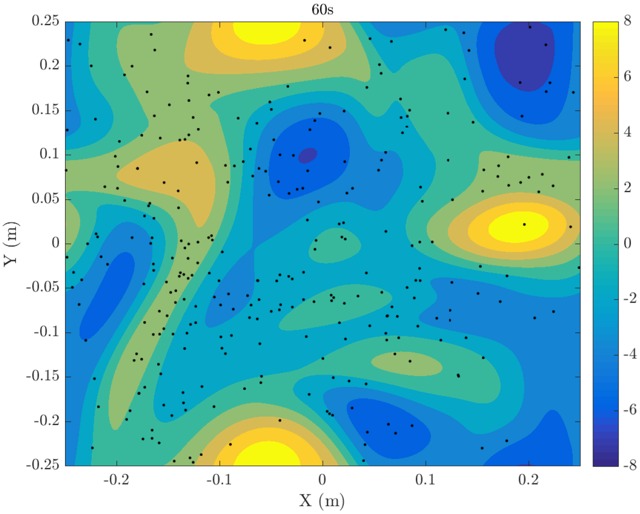

Figure 4.11: Instantaneous spatial distribution of cloud droplets (here $t = 60\,\mathrm{s}$). The contour map shows the corresponding vorticity distribution. The simulation corresponds to the $\bar{r}$ of the solid lines (2-D swarm model, pure collision driven by turbulence with Re ≈ 233) of Figure 4.6. Here, cloud droplets are plotted randomly.

swarm (Scheme II) model in a 3-D kinematic straining flow. When the amplitude of the straining flow is increased, as expected, the evolution of the mean radius reveals a peak shown in Figure 4.10. It is worth noting that in the straining flow, the growth of the mean radius shows some discrepancy (see Paper I) between the swarm model and the Eulerian model—starting already from the beginning, which we have not understood yet. One possible reason is that the swarm model neglects Brownian motion. If we introduce Brownian motion in the swarm model, the discrepancy may vanish, which is to be confirmed.

5. Conclusion and outlook

5.1 Conclusions

In this thesis, a preliminary investigation of turbulence effect on cloud droplet growth is conducted. Cloud droplet growth driven by collision in turbulent environment is a strongly nonlinear process. To get an idea about the solution of this problem, an Eulerian and two Lagrangian schemes are compared. We developed a numerical formulation for the Smoluchowski equation in multi-dimensions to investigate the bottleneck problem of cloud droplet growth. The condensation process is highly mass bin resolution demanding to reproduce the analytical solution. The collision process requires huge MBR to obtain a converged solution. Large artificial particle viscosities and Brownian diffusion coefficients are needed to stabilize the simulations in multi-dimensional cases, but they damp the growth of cloud droplets. Therefore the Lagrangian (swarm) scheme is preferred. The swarm scheme is more physical and practical in the sense that it allows for large stochastic effects and avoids the artificial particle viscosity. For the condensation process, the numerical solution of size spectra by the swarm model agrees well with the analytic one. For the collision process, the size spectra simulated by the Eulerian and swarm schemes agree well with each other at early times.

The combined condensational and collisional growths are simulated in a turbulent gas flow using the swarm model and the Euler model. Not only do the evolution of the mean size agree well with each other, but also the detailed inspection of the size spectra at early times. This sheds light on studying the strongly coupled collision process and turbulence. The size spectra become broadened with increasing Reynolds number. The evolution of the mean radius shows a counterintuitive but physical bump, which we explained through the dominance of coalescence of progressively larger particles. It is also related to turbulence-generated clustering.

5.2 Outlook

In Paper I we have simulated the condensation process using isotropic supersaturation, which is, however, strongly dependent on the ambient environment and it is desirable to have a system that allows for its spatial and temporal variations. The supersaturation can be simulated by coupled thermal dynamics and turbulence [28],

$$S(\boldsymbol{x},t) = \frac{q_v(\boldsymbol{x},t)}{q_{vs}(T)}, \tag{5.1}$$

where $q_{vs}(T)$ is the supersaturated vapor pressure at temperature T, $q_v(\boldsymbol{x},t)$ is the vapor mixing ratio and can be obtained by solving

$$\frac{\partial q_v}{\partial t} + \boldsymbol{u} \cdot \nabla q_v = D\nabla^2 q_v - C_d. \tag{5.2}$$

Here C_d is the condensation rate given by

$$C_d(\boldsymbol{x},t) = \frac{1}{m_a}\frac{dm_l(\boldsymbol{x},t)}{dt} = \frac{4\pi\rho_l G}{\rho_0 a^3}\sum_{\beta=1}^{\triangle} S\left(\boldsymbol{x}_\beta,t\right)a(t), \tag{5.3}$$

where m_a and m_l are the mass of air and liquid water, respectively, ρ_l and ρ_0 are the water density and the reference mass density of dry air, respectively, β denotes the grid cell and $\triangle$ is the total number of grid cells. To complete the equations, the temperature field needs to be solved by

$$\frac{\partial T}{\partial t} + \boldsymbol{u} \cdot \nabla T = \kappa\nabla^2 T + \frac{L}{c_p}C_d, \tag{5.4}$$

where κ is the thermal diffusion coefficient of air, c_p is the specific heat at constant pressure, and L is the latent heat. The condensation rate, given by Equation (5.3), is coupled with the cloud droplet radius and the supersaturation. Thus, together with Equation (2.1) and the momentum equation of the gas flow [see Equations (31)–(33) of Paper I], the supersaturation field can be solved. To conserve the mass of liquid water, we define the mixing ratio of total water as $q_{tot} = q_l + q_v$, where q_l is the mixing ratio of liquid water.

Another important shortcoming is the fact that in the present work, the collision efficiency is assumed to be perfect, resulting in unrealistically rapid growth. It should be considered in a future study. Furthermore, we only consider 2-D turbulence in the present study, which is another unphysical restriction. Extending our work to the 3-D case is straightforward and would be feasible particularly in the swarm model. Lastly, we would extend our study to the parameterization of LES [49] so that an appropriate representation of cloud droplet growth can be implemented in the LES. These will be parts of the topics to be addressed in the remaining period of my Ph.D. studies.

Acknowledgments

After two years of Ph.D. studies and research, it is time to express my genuine thanks to all persons who have ever helped and supported me.

I would like to express my heartfelt gratitude to my supervisors. I thank my supervisors for giving me the opportunity to do research at NORDITA & MISU. During the two years, Axel's enthusiasm and pursuit of great science and his view on science have impressed me a lot. I cannot forget the early mornings and late nights when we sat together to work on our project; I cannot forget the times when Axel and Gunilla helped me master the courses. Axel's research style and the attitude to life will be an invaluable fortune all through my future life. I want to thank Gunilla for her insightful suggestions on the project and her great patience for my course studies. Gunilla always encouraged me to do what I am interested in. I has been stimulated by Gunilla's insightful views of science. I would like to thank Nils, an amazing supervisor and collaborator. His intuition on physics and his grasp of DNS has inspired me a lot! My times in Trondheim with Nils were wonderful! Thank Igor Rogachevskii, Dhrubaditya, Lars and Nathan Kleeorin for useful discussions on this project. I would also like to thank all the senior researchers at MISU for their guidance.

Many thanks go to my committee meeting members, Kristofer and Linda, for their caring about my Ph.D. study. Thank the Astrophysics group of NORDITA. Thanks to Nishant and Sarah for everything, Harsha, Jennifer (Jenny) and Bidya for their help. I want to thank the Ph.D. students at MISU. I have wonderful time with you guys! My special thanks goes to Maartje, Lena, Waheeq, Georgia, Wing, Anna and Aitor. Thanks to my officemates Marin and Antonios for their tolerance of my "torturing" the keyboard. I would like to thank the administrative staff of NORDITA & MISU for their help. Special thanks go to Elizabeth, Hans, Anne and Mariana for their help. Thanks to Bonnie at LASP for taking care of my visa to the US.

Finally, I'm very grateful to my family. I'm greatly indebted to my parents. I haven't kept them company to enjoy the lunar year in the last five years. Parents are suffering from my working and studying far from home. I hope I can accompany them in the future.

Last but not least, I would like to express my thanks to the Research Council of Norway under the FRINATEK grant 231444 and the SeRC, through which my Ph.D. studies have been funded. Thank the Bolin Center for supporting part of the accommodation during my visit to the University of Colorado at Boulder.

References

[1] V. Ramanathan, R. D. Cess, E. F. Harrison, P. Minnis, B. R. Barkstrom, E. Ahmad, and D. Hartmann. Cloud-radiative forcing and climate: Results from the earth radiation budget experiment. *Science*, 243(4887):57–63, 1989. 1

[2] B. Stevens and S. Bony. What are climate models missing? *Science*, 340(6136):1053–1054, 2013. 1

[3] M. J. Beals, J. P. Fugal, R. A. Shaw, J. Lu, S. M. Spuler, and J. L. Stith. Holographic measurements of inhomogeneous cloud mixing at the centimeter scale. *Science*, 350(6256):87–90, 2015. 1, 3, 5, 22

[4] G. M. McFarquhar. A New Representation of Collision-Induced Breakup of Raindrops and Its Implications for the Shapes of Raindrop Size Distributions. *J. Atmosph. Sci.*, 61:777–794, 2004. 1

[5] R. A. Shaw. Particle-turbulence interactions in atmospheric clouds. *Ann. Rev. Fluid Mech.*, 35(1):183–227, 2003. 1

[6] E. Bodenschatz, S. P. Malinowski, R. A. Shaw, and F. Stratmann. Can we understand clouds without turbulence? *Science*, 327(5968):970–971, 2010. 1

[7] W. W. Grabowski and L.-P. Wang. Growth of cloud droplets in a turbulent environment. *Ann. Rev. Fluid Mech.*, 45:293–324, 2013. 1, 2

[8] D. Lamb and J. Verlinde. *Physics and Chemistry of Clouds*. Cambridge University Press, 2011. Cambridge Books Online. 1, 5, 6, 7, 9

[9] D. Arenberg. *Turbulence as the major factor in the growth of cloud drops*. Bull. Amer. Meteor., 1939. 1

[10] A. Gabilly. On the role that turbulence can play in the coalescence of cloud droplets. *Ann. Geophys*, 5:232–234, 1949. 1

[11] T. W. R. East and J. S. Marshall. Turbulence in clouds as a factor in precipitation. *Quart. J. Royal Met. Soc.*, 80(343):26–47, 1954. 1

[12] P. G. Saffman and J. S. Turner. On the collision of drops in turbulent clouds. *J. Fluid Mech.*, 1:16–30, 1956. 1, 9

[13] G. W. Reuter, R. De Villiers, and Y. Yavin. The collection kernel for two falling cloud drops subjected to random perturbations in a turbulent air flow: a stochastic model. *J. Atmosph. Sci.*, 45(5):765–773, 1988. 1

[14] L.-P. Wang and W. W. Grabowski. The role of air turbulence in warm rain initiation. *Atmosph. Sci. Lett.*, 10(1):1–8, 2009. 2

[15] O. Ayala, B. Rosa, and L.-P. Wang. Effects of turbulence on the geometric collision rate of sedimenting droplets. part 2. theory and parameterization. *New J. Phys.*, 10(9):099802, 2008. 2

[16] P. A. Vaillancourt, M. K. Yau, P. Bartello, and W. W. Grabowski. Microscopic approach to cloud droplet growth by condensation. part ii: Turbulence, clustering, and condensational growth. *J. Atmosph. Sci.*, 59(24):3421–3435, 2002. 2

[17] A. S. Lanotte, A. Seminara, and F. Toschi. Cloud droplet growth by condensation in homogeneous isotropic turbulence. *J. Atmosph. Sci.*, 66(6):1685–1697, 2009. 2, 5

[18] G. Sardina, F. Picano, L. Brandt, and R. Caballero. Continuous growth of droplet size variance due to condensation in turbulent clouds. *Phys. Rev. Lett.*, 115:184501, 2015. 2, 5

[19] J. Blum and G. Wurm. The growth mechanisms of macroscopic bodies in protoplanetary disks. *Ann. Rev. Astron. Astrophys.*, 46(1):21–56, 2008. 2

[20] K. Ros and A. Johansen. Ice condensation as a planet formation mechanism. *Astron. Astrophys.*, 552:A137, 2013. 2, 6

[21] The PENCIL CODE. `https://github.com/pencil-code`. 2

[22] W. R. Leaitch, G. A. Isaac, J. W. Strapp, C. M. Banic, and H. A. Wiebe. The relationship between cloud droplet number concentrations and anthropogenic pollution: Observations and climatic implications. *Journal of Geophysical Research: Atmospheres*, 97(D2):2463–2474, 1992. 3

[23] G. M. Martin, D. W. Johnson, and A. Spice. The measurement and parameterization of effective radius of droplets in warm stratocumulus clouds. *J. Atmosph. Sci.*, 51(13):1823–1842, 1994. 3

[24] A. K. Betts and M. J. Miller. A new convective adjustment scheme. part ii: Single column tests using gate wave, bomex, atex and arctic air-mass data sets. *Quart. J. Roy. Met. Soc.*, 112(473):693–709, 1986. 3

[25] D. H. Lenschow, I. R. Paluch, A. R. Bandy, R. Pearson Jr., S. R. Kawa, C. J. Weaver, B. J. Huebert, J. G. Kay, D. C. Thornton, and A. R. Driedger III. Dynamics and chemistry of marine stratocumulus (dycoms) experiment. *Bull. Am. Met. Soc.*, 69(9):1058–1067, 1988. 3

[26] J. Small, P. Chuang, and H. Jonsson. Microphysical imprint of entrainment in warm cumulus. *Tellus B*, 65(0), 2013. 3

[27] H. Xia, N. Francois, H. Punzmann, and M. Shats. Lagrangian scale of particle dispersion in turbulence. *Nat. Comm.*, 4, 2013. Article. 5

[28] B. Kumar, J. Schumacher, and R. A. Shaw. Lagrangian mixing dynamics at the cloudyâĂŞclear air interface. *J. Atmosph. Sci.*, 71(7):2564–2580, 2014. 5, 26

[29] E. X. Berry and R. L. Reinhardt. An analysis of cloud drop growth by collection: Part i. double distributions. *J. Atmosph. Sci.*, 31(7):1814–1824, 1974. 6

[30] W. D. Hall. A detailed microphysical model within a two-dimensional dynamic framework: Model description and preliminary results. *J. Atmosph. Sci.*, 37(11):2486–2507, 1980. 6

[31] J. Drazkowska, F. Windmark, and C. P. Dullemond. Modeling dust growth in protoplanetary disks: The breakthrough case. *Astron. Astrophys.*, 567:A38, 2014. 7, 9

[32] H. R. Pruppacher and J. D. Klett. *Microphysics of clouds and precipitation*. Kluwer Acadenic Publishers, 1998. 9

[33] A. Johansen, A. N. Youdin, and Y. Lithwick. Adding particle collisions to the formation of asteroids and kuiper belt objects via streaming instabilitiesâŃĘ. *Astron. Astrophys.*, 537:A125, 2012. 9, 10

[34] A. Zsom and C. P. Dullemond. A representative particle approach to coagulation and fragmentation of dust aggregates and fluid droplets. *Astron. Astrophys.*, 489(2):931–941, 2008. 10

[35] S. Shima, K. Kusano, A. Kawano, T. Sugiyama, and S. Kawahara. The super-droplet method for the numerical simulation of clouds and precipitation: a particle-based and probabilistic microphysics model coupled with a non-hydrostatic model. *Quart. J. Roy. Met. Soc.*, 135:1307–1320, 2009. 10

[36] J. H. Seinfeld and S. N. Pandis. *Atmospheric chemistry and physics: from air pollution to climate change*. John Wiley & Sons, 2012. 12

[37] G. Boffetta and R. E. Ecke. Two-dimensional turbulence. *Ann. Rev. Fluid Mech.*, 44(1):427–451, 2012. 16

[38] H. Siebert, K. Lehmann, M. Wendisch, H. Franke, R. Maser, D. Schell, E. Wei Saw, and R. A. Shaw. Probing finescale dynamics and microphysics of clouds with helicopter-borne measurements. *Bull. Am. Met. Soc.*, 87(12):1727–1738, 2006. 16

[39] P. G. Saffman and J. S. Turner. On the collision of drops in turbulent clouds. *J. Fluid Mech.*, 1:16–30, 1956. 22

[40] V. Dallas and J. C. Vassilicos. Rapid growth of cloud droplets by turbulence. *Phys. Rev. E*, 84:046315, 2011. 22

[41] L. R. Collins and A. Keswani. Reynolds number scaling of particle clustering in turbulent aerosols. *New J. Phys.*, 6(1):119, 2004. 22

[42] A. B. Kostinski and R. A. Shaw. Scale-dependent droplet clustering in turbulent clouds. *J. Fluid Mech.*, 434:389–398, 2001. 22

[43] W. C. Reade and L. R. Collins. Effect of preferential concentration on turbulent collision rates. *Phys. Fluids*, 12(10):2530–2540, 2000. 22

[44] V. E. Perrin and H. J. J. Jonker. Preferred location of droplet collisions in turbulent flows. *Phys. Rev. E*, 89:033005, 2014. 22

[45] V. E. Perrin and H. J. J. Jonker. Relative velocity distribution of inertial particles in turbulence: A numerical study. *Phys. Rev. E*, 92:043022, 2015. 22

[46] K. Gustavsson and B. Mehlig. Relative velocities of inertial particles in turbulent aerosols. *J. Turbulence*, 15(1):34–69, 2014. 22

[47] J. K. Eaton and J. R. Fessler. Preferential concentration of particles by turbulence. *Int. J. Multiphase Flow*, 20, Supp. 1:169 – 209, 1994. 22

[48] J. Bec, L. Biferale, M. Cencini, A. Lanotte, S. Musacchio, and F. Toschi. Heavy particle concentration in turbulence at dissipative and inertial scales. *Phys. Rev. Lett.*, 98:084502, 2007. 23

[49] J. Savre, A. M. L. Ekman, G. Svensson, and M. Tjernström. Large-eddy simulations of an arctic mixed-phase stratiform cloud observed during isdac: sensitivity to moisture aloft, surface fluxes and large-scale forcing. *Quart. J. Roy. Met. Soc.*, 141(689):1177–1190, 2015. 26

Eulerian and modified Lagrangian approaches to multi-dimensional condensation and coagulation

Xiang-Yu Li[1,2], A. Brandenburg[2,3,4], N. E. L. Haugen[5,6], and G. Svensson[1]

[1]*Department of Meteorology, and Bolin Centre for Climate Research, Stockholm University, Stockholm, Sweden*
[2]*Nordita, KTH Royal Institute of Technology and Stockholm University, 10691 Stockholm, Sweden*
[3]*Laboratory for Atmospheric and Space Physics, JILA and Department of Astrophysical and Planetary Sciences, University of Colorado, Boulder, CO 80303, USA*
[4]*Department of Astronomy, Stockholm University, SE-10691 Stockholm, Sweden*
[5]*SINTEF Energy Research, 7465 Trondheim, Norway*
[6]*Department of Energy and Process Engineering, NTNU, 7491 Trondheim, Norway*

Abstract

Turbulence is believed to play a crucial role in cloud droplet growth. It makes the collision process of inertial particles strongly nonlinear, which motivates the study of two rather different numerical schemes. Here, an Eulerian scheme based on the Smoluchowski equation is compared with two Lagrangian superparticle (or superdroplet) schemes in the presence of condensation and coagulation. The growth processes are studied either separately or in combination using either two-dimensional turbulence, a steady flow, or just gravitational acceleration without gas flow. Discrepancies between different schemes are most strongly exposed when condensation and coagulation are studied separately, while their combined effects tend to result in smaller discrepancies. In the Eulerian approach, the late growth of the mean particle radius slows down for finer mass bins, especially for collisions caused by different particle sizes. In the Lagrangian approach it is nearly independent of grid resolution at early times and weakly dependent at later times. However, the mean particle radius is shown to be of limited usefulness, because it tends to decrease when the largest particles out of a broad distribution coalesce. This can therefore result in a peak in the evolution of the mean particle radius, even though many droplets have already grown from cloud droplet (micrometer) to raindrop (millimeter) size. The Lagrangian schemes are generally found to be superior over the Eulerian one in terms of computational performance. However, it is shown that the use of interpolation schemes such as the cloud-in-cell algorithm is detrimental in connection with superparticle or superdroplet approaches. Furthermore, the use of symmetric over asymmetric coagulation schemes is shown to reduce the amount of scatter in the results.

Keywords: coagulation; condensation; cloud droplet formation; superdroplet approach; superparticle approach; size distribution spectra

Revision: 1.285

---

1. Introduction

In the context of raindrop formation, it is generally accepted that turbulence plays a crucial role in bridging the size gap between efficient condensational growth of small particles (radii below 10 μm) and efficient coagulational growth due to gravity of larger ones (radii around 100 μm

Preprint submitted to J. Comp. Phys. *April 28, 2016*

and above) [1, 2]. Solving this important problem in meteorology [3, 4, 5] might also shed light on how to bridge the even more severe size gap in the astrophysical context of planetesimal formation [6, 7]. To address these questions numerically, one has to combine direct numerical simulations (DNS) of turbulent gas motions with those of particles. The particles are cloud droplets in the meteorological context and dust grains in astrophysics. A possible approach to treating coagulation is to solve the Smoluchowski equation [8, 9], which couples the spatio-temporal evolution equations of the particle distribution function for different particle sizes. The particle motion can be treated using a fluid description for each particle size. Thus, not only does one have to solve the Smoluchowski equation at each meshpoint, but, because heavier particles have finite momenta and speeds that are different from those of the gas, one has to solve corresponding momentum equations for each mass species. This is an Eulerian approach, which is technically more straightforward than a Lagrangian one, but it becomes computationally demanding when the number of particle size or mass bins becomes large.

The Eulerian approach also has conceptual difficulties in that particles of the same size can never interact with each other owing to the fact that particles of the same size are described by the same momentum equation and have therefore the same velocity at a given position in space, so the mutual collision probability vanishes. This is not a problem for freely falling particles of the same size, which would have the same terminal velocity and would never collide anyway, but it would be an unrealistic restriction when particles are subjected to acceleration by turbulence.

An alternative approach is the Lagrangian one, where one solves for the motion of individual particles and treats collisions explicitly. In atmospheric clouds, the number density of micrometer-sized cloud droplets is of the order of $10^8\,\mathrm{m}^{-3}$, so in a volume of $1\,\mathrm{m}^3$, one has 100 million particles, which is the typical size that can still be treated on modern supercomputers. A domain of this size is also about the largest that is possible in direct numerical simulations (DNS) of atmospheric turbulence; the Reynolds number based on the length scale $\ell = 1$ m and the corresponding velocity scale $u_\ell \approx 0.2\,\mathrm{m/\,s}$ is $u_\ell\,\ell/\nu \approx 20,000$, where $\nu \approx 10^{-5}\,\mathrm{m}^2\,\mathrm{s}^{-1}$ is the viscosity of the gas flow. Such a large Reynolds number is just within reach on current supercomputers, but larger domains would remain out of reach for a long time. An intermediate approach involves the use of Lagrangian "superparticles" [7, 10, 11, 12], which represent a "swarm" of particles of certain size and number density. Depending on the values of particle size and number density, there is a certain probability that an encounter between two superparticles leads to coagulational growth of some of the particles in each swarm (or superparticle).

The purpose of the present paper is to compare the Eulerian approach involving the Smoluchowski equation with the Lagrangian superparticle approach with the aim of identifying a promising DNS scheme for tackling the bottleneck problem of cloud droplet growth. This has been done in the astrophysical context [13, 14], where the principal problem with the Eulerian approach was emphasized in that it requires high mass bin resolution (MBR) to avoid artificial speedup of the growth rate. Here we also compare with the superdroplet approach [11]. The original work on this approach was restricted to the case of vanishing particle inertia, but this restriction is not a principal limitation of this scheme, which is in fact well applicable to the case of finite particle inertia.

2. Lagrangian and Eulerian approaches

In the following, we refer to the superparticle or superdroplet approaches as the *swarm model*, where each superparticles represents a swarm of physical particles. By contrast, the Eulerian approach is also referred to as the *Smoluchowski model*. Here we compare the two approaches in the meteorological context of water droplets using, however, simplifying assumptions such as a constant supersaturation ratio and ideal collision efficiency. In this paper, we generally refer to particles and superparticles, which are thus used interchangeably with droplets and superdroplets, respectively.

2.1. The swarm model

The swarm model is a Monte Carlo type approach that handles particle collisions in a swarm of particles in a statistical manner [12]. Each swarm i has a particle number density n_i, and occupies a volume δx^D, which equals the volume of a fluid grid cell of size δx in D dimensions. All particles in a given swarm have the same mass, radius, and velocity. Following the description [7], the swarm is transported along with its "shepherd particle", which is also referred to as the corresponding superparticle. The swarm is treated as a Lagrangian point-particle, where one solves for the particle position $\boldsymbol{x}_i$ via

$$\frac{d\boldsymbol{x}_i}{dt} = \boldsymbol{V}_i \tag{1}$$

and the velocity via

$$\frac{d\boldsymbol{V}_i}{dt} = \frac{1}{\tau_i}(\boldsymbol{u} - \boldsymbol{V}_i) + \boldsymbol{g} \tag{2}$$

in the usual way. Here, $\boldsymbol{u}$ is the fluid velocity at the position of the swarm, $\boldsymbol{g}$ is the gravitational acceleration, τ_i is the particle inertial response or stopping time of a particle in swarm i and is given by

$$\tau_i = \frac{2\rho_d r_i^2}{9\rho\nu_i^{\mathrm{eff}}}, \tag{3}$$

where r_i is the radius of particles in swarm i, ρ_d is the particle solid material density and the effective viscosity is given by [15]

$$\nu_i^{\mathrm{eff}} = \nu\,(1 + 0.15\,\mathrm{Re}_i^{0.687}), \tag{4}$$

where ν is the ordinary (microphysical) fluid viscosity, and $\mathrm{Re}_i = 2r_i|\boldsymbol{u} - \boldsymbol{V}_i|/\nu$ is the particle Reynolds number, which provides a correction factor to the particle stopping time.

The growth of the particle radius r_i by condensation is governed by [16]

$$\frac{\mathrm{d}r_i}{\mathrm{d}t} = \frac{GS}{r_i}, \tag{5}$$

where S is the supersaturation ratio and G is the condensation parameter (having units of $\mathrm{m}^2\,\mathrm{s}^{-1}$). Both S and G are in principle dependent on the flow and the environmental temperature and pressure, but these dependencies are here neglected, because it would complicate the comparison of different numerical schemes even further. The assumed constancy of S also implies that the total liquid water content is not conserved.

A given swarm may only interact with every other swarm within the same grid cell. The computational cost associated with such collisions scales as N_{pg}^2, where N_{pg} is the number of swarms within a grid cell, but this is computationally not prohibitive as long as N_{pg} is not too large.

We now consider two swarms i and j residing within the same grid cell. Consider first collisions of particles within swarm j with a particle of swarm i. The inverse mean free path of i in j is given by

$$\lambda_{ij}^{-1} = \sigma_{ij} n_j E_{ij}, \tag{6}$$

where σ_{ij} is the collisional cross section with

$$\sigma_{ij} = \pi(r_i + r_j)^2, \tag{7}$$

and E_{ij} is the collision efficiency, but in the following we assume $E_{ij} = 1$ in all cases. The particle number density in swarm j is n_j and r_i and r_j represent the radii of the particles in the two swarms. From this, one can find the typical rate of collisions between a particle of swarm i and particles of swarm j as

$$\tau_{ij}^{-1} = \lambda_{ij}^{-1} \left|\boldsymbol{V}_i - \boldsymbol{V}_j\right| = \sigma_{ij} n_j \left|\boldsymbol{V}_i - \boldsymbol{V}_j\right| E_{ij}, \tag{8}$$

where $\boldsymbol{V}_i$ and $\boldsymbol{V}_j$ are the velocities of swarms i and j. The probability of a collision between the swarm i and any of the particles of swarm j within the current time step Δt is then given by

$$p_{ij} = \tau_{ij}^{-1} \Delta t. \tag{9}$$

This effectively puts a restriction on the time step, since the probability cannot be larger than unity. For each swarm pair in a grid cell, one now picks a random number, η_{ij}, and compares it with p_{ij}. A collision event occurs in the case when $\eta_{ij} < p_{ij}$.

2.2. *Coagulation scheme I*

For the swarm model, two different coagulation schemes have been proposed in the astrophysical and meteorological contexts. We begin discussing the former (scheme I), which is similar to that described in [7] in that it maintains a constant mass of the individual swarms. Scheme II is discussed in Section 2.3.

If $\eta_{ij} < p_{ij}$, one assumes that *all* the particles in swarm i have collided with a particle in swarm j. In this coagulation scheme, all swarms are treated individually. This means that even though the particles in swarm i have collided with the particles in swarm j, swarm j is kept unchanged at this stage. Instead, swarm j is treated individually at a different stage. Hence, all collisions are asymmetric, i.e., $p_{ij} \neq p_{ji}$. The new mass of the particles in swarm i now becomes

$$\tilde{m}_i = m_i + m_j, \tag{10}$$

where m_i is the mass before the collision and the tilde represents the new value after collision. In order to ensure mass conservation, the *total* mass of swarm i is kept unchanged, i.e.,

$$\tilde{n}_i \tilde{m}_i = n_i m_i, \tag{11}$$

which implies that the new particle number density, $\tilde{n}_i$, is given by $\tilde{n}_i = n_i m_i / \tilde{m}_i$. By invoking momentum conservation,

$$\tilde{\boldsymbol{V}}_i \tilde{m}_i = \boldsymbol{V}_i m_i + \boldsymbol{V}_j m_j, \tag{12}$$

the new velocity of any particle in swarm i is given by $\tilde{\boldsymbol{V}}_i = (\boldsymbol{V}_i m_i + \boldsymbol{V}_j m_j)/\tilde{m}_i$.

2.3. *Coagulation scheme II*

In the meteorological context, the following coagulation scheme has been proposed [11]. Assume two swarms i and j, and consider (without loss of generality) the case $n_j > n_i$. The collision probability of particles in swarm i with swarm j is, again, given by Eq. (9). If the two swarms are found to collide, the new masses of the particles in the two swarms are given by

$$\begin{aligned}\tilde{m}_i &= m_i + m_j,\\ \tilde{m}_j &= m_j,\end{aligned} \tag{13}$$

but now their new particle number densities are

$$\begin{aligned}\tilde{n}_i &= n_i,\\ \tilde{n}_j &= n_j - n_i.\end{aligned} \tag{14}$$

In other words, the number of particles in the smaller swarm remains unchanged (and their masses are increased), while that in the larger one is reduced by the amount of particles that have collided with all the particles of the smaller swarm (and their masses remain unchanged). Finally, the new momenta of the particles in the two swarms are given by

$$\begin{aligned}\tilde{\boldsymbol{V}}_i\tilde{m}_i &= \boldsymbol{V}_i m_i + \boldsymbol{V}_j m_j,\\ \tilde{\boldsymbol{V}}_j\tilde{m}_j &= \boldsymbol{V}_j m_j.\end{aligned} \tag{15}$$

In contrast to scheme I, these collisions are symmetric, i.e. $p_{ij} = p_{ji}$. Consequently, both swarms are changed during a collision.

2.4. Initial particle distribution

We recall that particles within a swarm may interact with particles of another swarm only if both swarms occupy the same grid cell. The effective volume of each swarm is therefore equal to δx^D, where D is the spatial dimension introduced in Section 2.1. The total number of particles in our computational domain is therefore δx^D times the sum of n_i over all N_p swarms. This must also be equal to nL^D, where n is the total number density represented by the simulation and L is the size of the computational domain. Thus, we have

$$nL^D = \delta x^D \sum_{i=1}^{N_p} n_i. \tag{16}$$

Initially ($t = 0$), the particle number densities of all swarms are the same and since $(L/\delta x)^D = N_{\rm grid}$ is the total number of grid points, we have $nN_{\rm grid} = n_i N_p$. Thus, the initial number density of particles within one swarm must be

$$n_i = nN_{\rm grid}/N_p \quad (\text{at } t = 0). \tag{17}$$

In the following, we choose the initial particle size distribution to be log-normal, i.e.,

$$f(r_i) = \left(n\Big/\sqrt{2\pi}\sigma_{\rm p}\right)\exp\left\{-[\ln(r_i/r_{\rm ini})]^2/2\sigma_{\rm p}^2\right\}, \tag{18}$$

where $r_{\rm ini}$ and $\sigma_{\rm p}$ are the center and width of the size distribution, respectively.

2.5. Eulerian approach

To model the combined growth of particles through condensation and coagulation in a multi-dimensional flow in the Eulerian description, we describe the evolution of particles of different radii r (or, equivalently, of different logarithmic particle mass $\ln m$) at different positions $\boldsymbol{x}$ and time t. We employ the particle distribution function $f(\boldsymbol{x}, r, t)$, or, alternatively in terms of logarithmic particle mass $\ln m$, $\tilde{f}(\boldsymbol{x}, \ln m, t)$, such that the total number density of particles is given by

$$n(\boldsymbol{x}, t) = \int_0^\infty f(\boldsymbol{x}, r, t)\,\mathrm{d}r, \tag{19}$$

or, correspondingly for $\tilde{f}$, we have $n(\boldsymbol{x}, t) = \int_{-\infty}^{\infty} \tilde{f}(\boldsymbol{x}, \ln m, t)\,\mathrm{d}\ln m$. Since $m = 4\pi r^3 \rho_\mathrm{d}/3$, we have $\tilde{f} = f\,\mathrm{d}r/\mathrm{d}\ln m = fr/3$. Note that $n(\boldsymbol{x}, t)$ obeys the usual continuity equation,

$$\frac{\partial n}{\partial t} + \boldsymbol{\nabla}\cdot(n\boldsymbol{v}) = D_\mathrm{p}\nabla^2 n, \tag{20}$$

where D_p is a Brownian diffusion term, which is enhanced for numerical stability and will be chosen depending on the mesh resolution. The evolution of the particle distribution function is governed by a similar equation, but with additional coupling terms due to condensation and coagulation, i.e.

$$\frac{\partial f}{\partial t} + \boldsymbol{\nabla}\cdot(f\boldsymbol{v}) + \nabla_r(fC) = \mathcal{T}_\mathrm{coag} + D_\mathrm{p}\nabla^2 f, \tag{21}$$

where $\nabla_r = \partial/\partial r$ is the derivative with respect to r, $C = 3GS/r^2$ quantifies the rate of condensation, and $\mathcal{T}_\mathrm{coag}$ describes the change of the number density of particles for smaller and larger radii, as will be defined below. Furthermore, $\boldsymbol{v}(\boldsymbol{x}, r, t)$ is the particle velocity within the resolved grid cell and is, in turn, affected by gravity and, more importantly, by the friction force with the gas. The degree of coupling depends on the value of τ_i given by Eq. (3).

The modeling of condensation and coagulation implies coupling of the evolution equations of $f(\boldsymbol{x}, r, t)$ for different values of r. The advantage of using $\tilde{f}(\boldsymbol{x}, \ln m, t)$ is that it allows us to cover a large range in m, because we will use then an exponentially stretched grid in m such that $\ln m$ is uniformly spaced [17, 18]. The total number density within a finite mass interval $\delta \ln m$ is then given by $\tilde{f}(\boldsymbol{x}, \ln m, t)\,\delta\ln m$. Thus, the total number density of particles of all sizes at position $\boldsymbol{x}$ and time t is given by

$$n(\boldsymbol{x}, t) = \sum_{k=1}^{k_\mathrm{max}} \tilde{f}_k\,\delta\ln m = \sum_{k=1}^{k_\mathrm{max}} \hat{f}_k, \tag{22}$$

where $\hat{f}_k = \tilde{f}(\ln m_k)\,\delta\ln m$ is the variable used in the simulations and k_max is the number of logarithmic mass bins.

Let us first consider the process of condensation, which is described in Eq. (21) by the term $\nabla_r(fC)$, where fC is the flux of particle from one size bin to the next. Evidently, the total number density is only conserved if the particle flux fC vanishes for $r = r_\mathrm{min}$ and $r = r_\mathrm{max}$, which is the case if the range of r is sufficiently large. In particular, $(fC)_\mathrm{min} \to 0$, because $n \to 0$ for $m \to 0$. In practice, however, we consider finite lower cutoff values of m and therefore expect some degree of mass loss at the smallest mass bins. The same is also true for the largest mass bin once the size distribution has grown to sufficiently large values. In all cases with pure condensation, it is convenient to display solutions in non-dimensional form by measuring time in units of

$$\tau_\mathrm{cond} = r_\mathrm{ini}^2/2GS \tag{23}$$

and r in units of $r_{\rm ini}$. We refer to Appendix A for more details on the condensation equation for the Eulerian approach.

Next, we consider coagulation, which leads to a decrease of n, but does not change the mean mass density of liquid water. The evolution of $\tilde{f}(\boldsymbol{x}, \ln m, t)$ due to coagulation is governed by the Smoluchowski equation

$$\begin{aligned}\mathcal{T}_{\rm coag} = \tfrac{1}{2}\int_0^m K(m-m', m')\, f(m-m')\, f(m')\, \mathrm{d}m' \\ - \int_0^\infty K(m, m')\, f(m)\, f(m')\, \mathrm{d}m'. \qquad (24)\end{aligned}$$

Here, K is a kernel, which is proportional to the collision efficiency $E(m, m')$ and a geometric contribution. As mentioned above, we assume $E = 1$ and so K is given by

$$K(m, m') = \pi(r + r')^2 |\boldsymbol{v} - \boldsymbol{v}'|, \qquad (25)$$

where r and r' are the radii of the corresponding mass variables, m and m', while $\boldsymbol{v}$ and $\boldsymbol{v}'$ are their respective velocities.

In the following, we define the mass and radius bins such that

$$m_k = m_1 \delta^{k-1}, \quad r_k = r_1 \delta^{(k-1)/3}. \qquad (26)$$

Unfortunately, $\delta = 2$ is in many cases far too coarse, so we take

$$\delta = 2^{1/\theta}, \qquad (27)$$

where θ is chosen to be a power of two. In terms of $\hat{f}_k$, Eq. (24) reads

$$\mathcal{T}_k^{\rm coag} = \tfrac{1}{2} \sum_{i+j \in k} K_{ij} \hat{f}_i \hat{f}_j - \hat{f}_k \sum_{j=1}^{k_{\max}} K_{ik} \hat{f}_i, \qquad (28)$$

where we have adopted the nomenclature of Johansen [18] where $i + j \in k$ denotes all values of i and j for which

$$m_{k-1/2} \leq m_i + m_j < m_{k+1/2} \qquad (29)$$

is fulfilled. The discrete kernel is then $K_{ij} = \pi(r_i + r_j)^2 |\boldsymbol{v}_i - \boldsymbol{v}_j|$. The corresponding momentum equations for the velocities $\boldsymbol{v}_k(\boldsymbol{x}, t) = \boldsymbol{v}(\boldsymbol{x}, \ln m_k, t)$ for each logarithmic mass value $\ln m_k$ is

$$\frac{\partial \boldsymbol{v}_k}{\partial t} + \boldsymbol{v}_k \cdot \boldsymbol{\nabla} \boldsymbol{v}_k = \boldsymbol{g} - \frac{1}{\tau_k}(\boldsymbol{v}_k - \boldsymbol{u}) + \boldsymbol{F}_k(\boldsymbol{v}_k), \quad 1 \leq k \leq k_{\max}. \qquad (30)$$

Here, $\boldsymbol{u}$ is the gas velocity, τ_k (for $k = i$) is defined by Eq. (3), and $\boldsymbol{F}_k(\boldsymbol{v}_k) = \nu_p \nabla^2 \boldsymbol{v}_k$ is a viscous force, which should be very small for dilute particle suspensions, but is nevertheless retained in Eq. (30) for the sake of numerical stability of the code. In principle, the expression for $\boldsymbol{F}_k(\boldsymbol{v}_k)$ should be based on the divergence of the traceless rate-of-strain tensor of $\boldsymbol{v}_k$, similarly to the corresponding expression for the viscous force of the gas discussed below. However, since the term $\boldsymbol{F}_k(\boldsymbol{v}_k)$ is unphysical anyway, we just use the simpler expression proportional to $\nabla^2 \boldsymbol{v}_k$ instead.

2.6. Evolution equations for the gas flow in both approaches

To obtain $\boldsymbol{u}$ at each meshpoint, we solve the usual Navier-Stokes equation

$$\frac{\partial \boldsymbol{u}}{\partial t} + \boldsymbol{u} \cdot \boldsymbol{\nabla} \boldsymbol{u} = \boldsymbol{f} - \rho^{-1} \boldsymbol{\nabla} p + \boldsymbol{F}(\boldsymbol{u}), \tag{31}$$

where $\boldsymbol{f}$ is a forcing term, p is the gas pressure, ρ is the gas density, which in turn obeys the continuity equation,

$$\frac{\partial \rho}{\partial t} + \boldsymbol{\nabla} \cdot (\rho \boldsymbol{u}) = 0, \tag{32}$$

the viscous force $\boldsymbol{F}(\boldsymbol{u})$ is given by

$$\boldsymbol{F}(\boldsymbol{u}) = \nu(\nabla^2 \boldsymbol{u} + \tfrac{1}{3} \boldsymbol{\nabla\nabla} \cdot \boldsymbol{u} + 2\mathbf{S} \cdot \boldsymbol{\nabla} \ln \rho), \tag{33}$$

where $S_{ij} = \frac{1}{2}(u_{i,j} + u_{j,i}) - \frac{1}{3}\delta_{ij} \boldsymbol{\nabla} \cdot \boldsymbol{u}$ is the traceless rate-of-strain tensor and commas denote partial differentiation. We assume that the gas is isothermal and has constant sound speed $c_{\rm s}$ so that the pressure $p = c_{\rm s}^2 \rho$ is proportional to the gas density ρ. Note that gravity has been neglected in Eq. (31), but this is not a principal restriction and can be relaxed once suitable non-periodic boundary conditions are adopted. For the relatively small domains that can be handled by DNS, gravity will nevertheless have only minor effects on the fluid flow for atmospheric conditions.

To obtain a non-vanishing flow, we apply volume forcing via the term $\boldsymbol{f}$. In the case of a time-independent two-dimensional (2-D) divergence-free straining flow,

$$\boldsymbol{u}_{\rm str} = u_0\,(\sin kx \cos kz, 0, -\cos kx \sin kz), \tag{34}$$

we take $\boldsymbol{f} = \nu k^2 \boldsymbol{u}_{\rm str}$, where, u_0 determines the amplitude and k the wavenumber of the flow. Alternatively, we also consider a kinematic flow where we set $\boldsymbol{u} = \boldsymbol{u}_{\rm str}$. In the case of a turbulent flow, $\boldsymbol{f}$ is delta-correlated in time and consists of random waves in space [19]. The flow is characterized by a typical forcing wavenumber $k_{\rm f}$ ($\sqrt{2}k$ for the straining flow or the average wavenumber from a narrow band of wavevectors) and the root-mean-square (rms) velocity $u_{\rm rms}$. As a relevant timescale characterizing such a flow, we define

$$\tau_{\rm cor} = (u_{\rm rms} k_{\rm f})^{-1}, \tag{35}$$

which is an estimate of the correlation time. This definition is also used for the straining flow, which is a special case in that it is time-independent and therefore $\tau_{\rm cor}$ would no longer characterize the correlation time of the flow, but it would still be proportional to the turnover time.

2.7. Boundary conditions and diagnostics

In the present work, we use periodic boundary conditions for all variables in all directions. Therefore, no particles and no gas are lost through the boundaries of the domain. The use of periodic boundary conditions requires us to neglect gravity in Eq. (31), which could be relaxed if non-periodic boundary conditions were adopted.

To characterize the size distribution, especially for the larger particles, we consider the evolution of different normalized moments of the size spectra,

$$a_\zeta = \left(\int \tilde{f}(\ln m)\, r^\zeta \,\mathrm{d}\ln m \bigg/ \int \tilde{f}(\ln m)\,\mathrm{d}\ln m \right)^{1/\zeta}. \tag{36}$$

The mean radius $\bar{r}$ is given by a_1. Higher moments represent the wings of the distribution at large radii.

In the case of coagulation, the condensation timescale $\tau_{\rm cond}$, defined in Eq. (23), is no longer relevant, but it is instead a coagulation timescale that can be defined in the Eulerian model as

$$\tau_{\rm coag}^{-1} = \sum_{k=1}^{k_{\max}} \left\langle \mathcal{T}_k^{\rm coag} \right\rangle \bigg/ \sum_{k=1}^{k_{\max}} \left\langle \hat{f}_k \right\rangle, \tag{37}$$

which is, in this definition, a time-dependent quantity. Here, angle brackets denote volume averaging. In the Lagrangian model, this quantity can be defined by the collision frequency. Unlike the case of pure condensation, where $\tau_{\rm cond}$ was used as the appropriate time unit, $\tau_{\rm coag}$ can only be used a posteriori as a diagnostic quantity. However, given that the speed of pure coagulation is proportional to the mean particle density n, it is often convenient to perform simulations at increased values of n and then rescale time to a fixed reference density n_0 and use

$$\tilde{t} = t\, n/n_0. \tag{38}$$

In the following we use $n_0 = 10^8\,{\rm m}^{-3}$, which is the typical value of n in atmospheric clouds. Analogously we also define $\tilde{\tau}_{\rm coag} = \tau_{\rm coag}\, n/n_0$.

As mentioned above, a shortcoming of the Eulerian approach is that no coagulation is possible from equally sized particles. To assess the consequences of this unphysical limitation, we study the sensitivity of the results to replacing $K_{i\,i}$ either (i) by $(K_{i+1\,i} + K_{i\,i+1})/2$ or (ii) by $\epsilon_{\rm self}\pi(2r_i)^2|\boldsymbol{v}_i + \boldsymbol{v}_j|/2$, where $\epsilon_{\rm self}$ is an empirical parameter.

2.8. Computational implementation

We use the Pencil Code[1], which is a public domain code where the relevant equations have been implemented [18, 20, 21]. We refer to Appendix A for a description of an important modification applied to the implementation of Eq. (5), which is available with revision 722883 and later. The implementation of Eq. (28) has been discussed in detail by Johansen [18], and follows an approach described earlier [17]. It avoids inaccuracies resulting from the fact that for logarithmic mass binning, mass conservation cannot be accurately obeyed unless one redefines the mass bins dynamically at each mesh point. Although this formulation has been implemented [18], we found that the resulting departures from mass conservation were acceptably small and did therefore not invoke this refinement.

3. Results

3.1. Homogeneous condensation and coagulation experiments

We first consider the homogeneous case in which there is no spatial variation of the velocity and density fields for both the gas and the particles. We compare the Eulerian and Lagrangian models separately for pure condensation and coagulation processes.

---

[1] http://pencil-code.github.com/

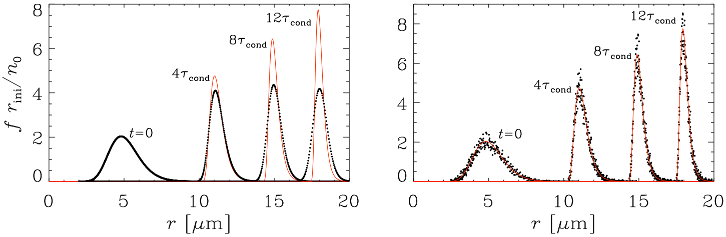

Figure 1: Comparison between numerical solution of size spectra and analytic solution for condensation for a lognormal initial conditions given by $n_0 = 10^8\,\mathrm{m}^{-3}$, $r_{\rm ini} = 5\,\mu$m, and $\sigma = 0.2$. Simulations of pure condensation (no turbulence nor gravity) with the Eulerian model using $\theta = 128$ and 1281 mass bins in the range 2–20 μm (left panel) and the Lagrangian swarm model with $N_p = 10000$ and $N_{\rm grid} = 16^3$ (right panel). The solid lines correspond to the analytic solution given by Eq. (40) while the black dots represent the numerical results.

3.1.1. Homogeneous condensation

In the case of homogeneous condensation, we can compare the numerical solution with the analytic solution of [22]; see their Fig. 13.25. To this end, we make use of the fact that solutions of the condensation equation (5) obey

$$f(r,t) = (r/\tilde{r})\, f(\tilde{r},0), \tag{39}$$

where $\tilde{r}$ is a shifted coordinate with $\tilde{r}^2 = r^2 - 2GSt$. With the log-normal initial distribution given by Eq. (18), this yields

$$f(r,t) = \frac{n}{\sqrt{2\pi}\,\sigma_{\rm p}}\frac{r}{\tilde{r}^2}\exp\left[-\frac{(\ln\tilde{r} - \ln r_{\rm ini})^2}{2\sigma_{\rm p}^2}\right], \tag{40}$$

where $r_{\rm ini}$ denotes the position of the peak of the distribution and $\sigma_{\rm p} = \ln\sigma_{\rm SP}$ denotes its width, where $\sigma_{\rm SP}$ is the symbol introduced in Ref. [22]. What is remarkable here is the fact that $f(r,t)$ vanishes for $r < r_* \equiv \sqrt{2GSt}$ and that $\partial f/\partial r$ has a discontinuity at $r = r_*$. This poses a challenge for the Eulerian scheme in which the derivative $\partial/\partial r$ is discretized; see Eq. (21). In Figure 1, we compare solutions obtained using both Eulerian and Lagrangian approaches. It is evident that the r-dependence obtained from the Eulerian solution is too smooth compared with the analytic one, even though we have here used 1281 points to represent r on our logarithmically spaced mesh over the range $2\,\mu\mathrm{m} \le r \le 20\,\mu$m with $\theta = 128$, so $\delta \approx 1.0054$; see Eq. (27). Better accuracy could be obtained by using a uniformly spaced grid in r, but this would not be useful later when the purpose is to consider coagulation spanning a range of several orders of magnitude in radius. By comparison, the Lagrangian solution shown in the right hand panel of Figure 1 (here with $n = 10^{10}\,\mathrm{m}^{-3}$) has no difficulty in reproducing the discontinuity in $\partial f/\partial r$ at $r = r_*$.

In practice, we would use logarithmic spacing on a mesh with $\delta = 2$ or $2^{1/2} \approx 1.414$. However, in such cases, the distribution develops broad wings. This can be seen by plotting the evolution of different moments a_ζ. In Figure 2 we show $(a_{24}/r_{\rm ini})^2$ for different mass bin resolutions θ and compare with $(\bar{r}/r_{\rm ini})^2$. In the Eulerian model, we consider the values $\theta = 2$, 8, and 128 over the mass bin interval 2–20 μm, so the number of bins are $k_{\rm max} - 1 = 20$, 80, and 1280,

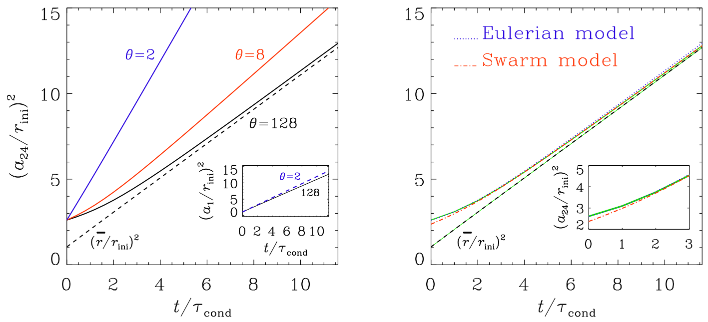

Figure 2: Comparison of $(a_{24}/r_{\rm ini})^2$ for $\theta = 2$ (blue), 8 (red), and 128 (black solid) for condensation, together with $(\overline{r}/r_{\rm ini})^2$ for $\theta = 128$ (black dashed) using the mass bin interval 2–20 μm. The inset shows $(a_1/r_{\rm ini})^2$ for $\theta = 2$ (blue dashed) and 128 (solid black). The right panel shows a comparison of the 24th moment between the Eulerian model with 1281 mass bins (blue dotted) and the swarm model with coagulation scheme I, $N_p = 10,000$, and $N_{\rm grid} = 16^3$ (red). The solid green lines show the analytic solutions for a_1 and a_{24}. The latter is shown more clearly in the inset. The black dashed line shows $(a_1/r_{\rm ini})^2$ for $\theta = 128$ and agrees nearly perfectly with the analytic result (thin green line). Here, the parameters for condensation and the initial conditions are the same as for Figure 1.

respectively. In the Lagrangian model, we use $N_p = 10,000$ and $N_{\rm grid} = 16^3$, so $N_p/N_{\rm grid} \approx 2.4$. At higher resolution, the a_ζ for different values of ζ converge to the same value, but not at low resolution (see inset). This can have a lasting effect on the growth of the higher moments in the sense that the slope in Figure 2 is increased at all later times. This is consistent with earlier findings [13, 14]. When coagulation is included, the artificially broadened tails in the distribution can be particularly dangerous, because they would have a strong effect on the rate of coagulation, which would be faster when the a_ζ for large values of ζ are increased by the artificially broadened size distribution. In the right hand panel of Figure 2, we compare $(a_{24}/r_{\rm ini})^2$ for both the swarm model and the high resolution Eulerian simulation. From this it is clear that the swarm model reproduces the high resolution Eulerian simulation rather accurately.

3.2. Purely gravitational coagulation experiments

For the purely geometrical kernel, no analytic solution exists. However, we can compare the convergence properties of our two quite different numerical approaches and thereby get some sense of their validity in cases when the two agree. Here we consider pure coagulation experiments, starting again with a log-normal distribution. The results are presented in terms of normalized time; see Eq. (38).

3.2.1. Eulerian approach

The MBR dependency of the numerical solution using the Smoluchowski scheme appears to be a serious obstacle in studying particle growth not only by condensation but also by coagulation. In Figure 3, we compare the evolutions of a_1 and a_3 using different MBR and thus different values of θ. We also considered the evolution of a_6, but it was very similar to that of a_3 in that the Eulerian solutions for different resolutions agreed quite well with each other and with the

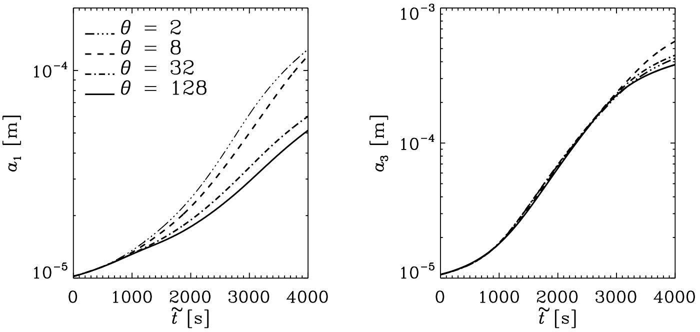

Figure 3: Evolution of the normalized moments a_1 and a_3 for simulations with gravity but no condensation nor turbulence. The different black lines represent simulations with different number of mass bins (solid line: $k_{\max} = 3457$ with $\theta = 128$, dashed-dotted line: $k_{\max} = 865$ with $\theta = 32$, dashed line: $k_{\max} = 217$ with $\theta = 8$, and dashed-triple-dotted line: $k_{\max} = 55$ with $\theta = 2$).

solution from the swarm model. For a_1 the evolutions are strongly MBR dependent. Nevertheless, the evolution of a_3 with different MBR converges over a wide range of MBR spanning from $k_{\max} = 55$–3457. We also tested the MBR dependency using a constant kernel. In that case, it turns out that the results converge only for $k_{\max} \geq 50$. However the geometrical kernel combined with the Smoluchowski equation is strongly nonlinear. Therefore, a_1 converges only for even larger MBR in the case of purely gravity-driven collision, which is a strong argument in favor of the Lagrangian scheme.

3.2.2. Comparison between swarm coagulation schemes I and II

In Figure 4, the same variables as in Figure 3 are shown, but now the swarm model is used. The simulations have been performed with 32^3 grid points and different average numbers of swarm particles per grid point ($N_p/N_{\rm grid} = 2$–8). It can be seen from the plots that the swarm simulations with coagulation scheme II almost converge for $N_p/N_{\rm grid} = 4$. It is also seen that the results from the swarm simulations with the highest number of swarms follow the Smoluchowski results rather well for a_3 (right hand panel), while the results for a_1 (left panel) depart at later times. Moreover, for a_1 the results of the swarm simulations with scheme I agree with those of scheme II at early times, but depart at late times. However, for a_3, the agreement is good. The evolution of a_1 with scheme I shows considerable scatter at late times. We recall that the main difference between schemes I and II is the geometry of collision. Collisions simulated with scheme I are asymmetric, while those with scheme II are symmetric. Thus, in scheme II both swarms change either their total mass or their total particle number, while in scheme I the total mass of a swarm is kept constant by adjusting the particle number correspondingly. This may be responsible for creating stronger fluctuations in the mean radius. Therefore, to keep the amount of scatter comparable, scheme II is effectively less demanding. In the following, we will mainly

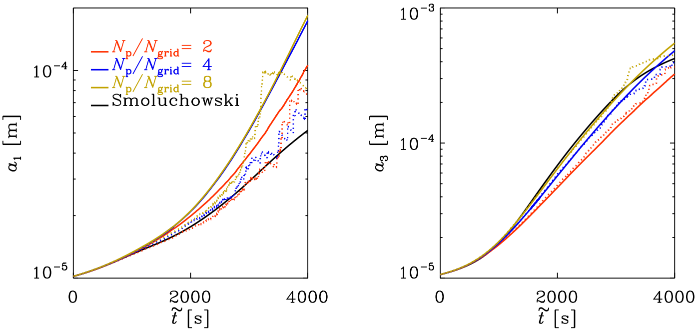

Figure 4: Similar to Figure 3, but for 3-D simulations with the swarm model and 32^3 grid points. The different colors represent simulations with different mean number of swarms per grid point ($N_p/N_{\rm grid}$). Dashed lines represent simulations with scheme I and the solid ones represent simulations with scheme II. The total number density of physical particles are kept the same for all simulations by changing the number density of particles in each swarm.

adopt scheme II to save computational time. At early times, on the other hand, the evolution of $\bar{r}$ obtained from the swarm model with coagulation scheme I follows more closely that of the Eulerian model.

From Figure 5 it can be seen that for three-dimensional (3-D) simulations with $N_p/N_{\rm grid} = 4$, the results are more or less converged when the total number of swarms reaches 128×10^3. Since all fluid variables are constant in these simulations with no gas flow, the number of grid points has no effect on the fluid. The number of swarms can therefore be changed by increasing the total number of grid points while maintaining $N_p/N_{\rm grid} = 4$.

3.2.3. Size spectra

The evolution of size spectra in the Smoluchowski simulation with 3457 mass bins, $\theta = 128$, and coagulation scheme II (same case as in Figure 4) is shown as black lines in Figure 6, while the corresponding size spectra obtained with simulations utilizing the swarm model with 8 and 32 particles per grid point are shown in the left-hand panel. The agreement between the Eulerian and Lagrangian schemes is good at early times, but at late times the size spectra from the Eulerian approach develop an excess for the largest sizes ($r_{\rm max} = 1000\,\mu$m) and yield deficient values at intermediate sizes (30–300$\,\mu$m).

It is interesting to note that, when the swarm model is used in a one-dimensional (1-D) simulation, the agreement between the Smoluchowski and swarm approaches is better, as can be seen from the right-hand panel of Figure 6. This can be explained by the fact that a given swarm particle in a 1-D simulation with pure gravity can have all the other swarm particles in the simulation as collision partners, while for a 3-D simulation with pure gravity a given swarm particle can only collide with another swarm particle within the same $1 \times 1 \times 32$ vertical columns of grid points. This inevitably reduces the statistics in the 3-D simulations. For turbulent cases,

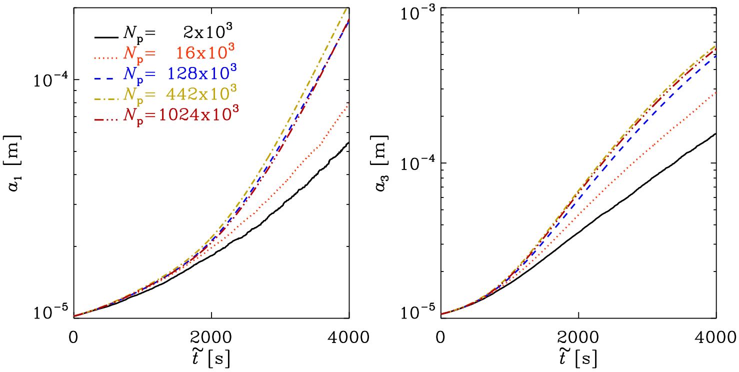

Figure 5: Same as Figures 3 and 4 but for $N_p/N_{\rm grid} = 4$. The different colors represent simulations with different total numbers of swarms. The corresponding $N_{\rm grid}$ is 8^3 (black solid curve), 16^3 (red dotted curve), 32^3 (blue dashed curve), 48^3 (orange dash-dotted curve) and 64^3 (dark red dash-three-dotted curve).

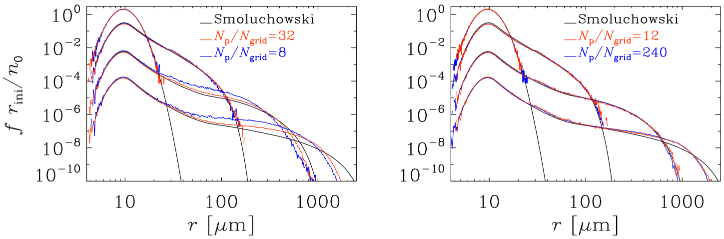

Figure 6: Size spectra for three different runs at times $\tilde{t} = 0$ s, 2000 s and 4000 s. The black line correspond to the highest resolution Smoluchowski simulation while the red and blue lines represents results from the swarm model with 32^3 grid points in 3-D (left panel) and with 4096 grid points in 1-D (right panel).

this is not expected to be important since the turbulence will move the particles out of their initial vertical column, making all particles a potential collision partner even in 3-D.

We emphasize that the mean radius is sensitive to subtle changes in the size distribution, but it is at the same time not really relevant to characterizing the coagulation of large particles. This can be seen in the fact that the mean particle radius often increases by not much more than a factor of three (see the left-hand panel of Figure 3), while the size distribution can become rather broad and its tail can reach the size of raindrops (see Figure 6) within a relatively short time. In addition, the evolution of the mean radius reaches a peak in the inhomogeneous coagulation process, as will be discussed in Section 3.3. Instead of the mean radius, we will therefore adopt the size

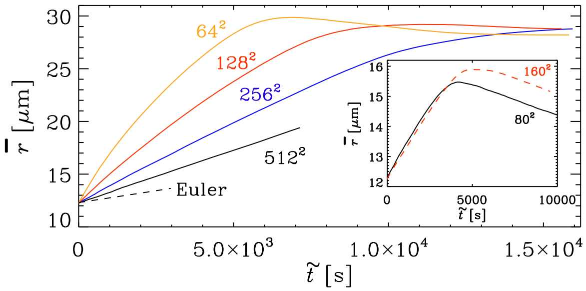

Figure 7: Comparison of the evolution of the mean particle size in a straining flow for simulations with the swarm approach at different resolutions. Here, both condensation and coagulation are included and the CIC particle interpolation algorithm has been used. The total number of swarms is here $N_p = 300,000$. The inset shows the case with NGP mapping instead of the CIC second order interpolation for particle properties.

spectra and the higher moments to address the coagulation of large particles. Nevertheless, the mean radius will still be used as a criterion for comparison between the Eulerian and Lagrangian models.

3.3. Inhomogeneous coagulation in a straining flow

Spatial variation in the flow leads to local concentrations and thus to large peak values of $f(\boldsymbol{x}, r, t)$ that shorten the coagulation time τ_{coag} [23]. Before studying the turbulent case, we consider first coagulational growth in a steady two-dimensional (2-D) divergence-free straining flow. The straining flow is numerically inexpensive and easy to control and analyze compared with turbulence. However, given that it is a steady flow, the particles will end up near the vertices of converging flow vectors and will therefore be much more concentrated in the swarm model than what is possible to represent in the Eulerian model.

3.3.1. Pure coagulation

We consider first the case of pure coagulation. In Figure 7 we show the time-dependence of $\overline{r}$ for the swarm model with coagulation scheme II at different resolutions ranging from 64^2 to 512^2 meshpoints. (Here, we used $\boldsymbol{f} = \nu k^2 \boldsymbol{u}_{\text{str}}$, whereas in all other cases, including the inset of Figure 7, we used $\boldsymbol{u} = \boldsymbol{u}_{\text{str}}$ as a kinematic flow, but the differences are negligible.) Surprisingly, $\overline{r}$ grows more slowly as we increase the mesh resolution of the swarm model. In the Eulerian model, on the other hand, it grows slower still. Given that the swarm models seem to converge toward the Eulerian model, we are confronted with the question of what causes the growth of $\overline{r}$ in the swarm model to slow down at higher mesh resolution. In this connection, we must emphasize that by default we use a second order interpolation to evaluate the gas properties at the position of each Lagrangian particle. This will play an important role, as will be discussed now.

When traditional point particle Lagrangian particle tracking is employed, it is usually beneficial to employ higher order interpolation between the neighboring grid cells to find the value of a given fluid variable at the exact position of the particle. In the swarm approach, however, the particles in each swarm are filling up the entire volume of the grid cell in which the shepherd particle is. The distribution of the swarm throughout the grid cell is homogeneous and isotropic, and as such the swarm has no particular position within the grid cell. It is true that there is a particular position associated with the swarm, namely the position of the shepherd particle, but this position has no purpose other than to determine in which grid cell the swarm resides. We must therefore conclude that it is *n*ot better to use any kind of interpolation in determining the value of the fluid variables at the position of the swarm, but rather to use the values of the grid cell in which the swarm resides. This method is technically referred to as nearest grid point mapping (NGP). This is an important point, and the coagulation speed can be greatly exaggerated if interpolation is used.

The example shown in Figure 7 demonstrates the artificial speedup of the coalescence with increasing volume of the grid cells. Here, the cloud-in-cell (CIC) algorithm is used. The reason for the increased coagulation rate experienced when interpolation is used can be understood by considering two swarms consisting of tracer particles, i.e. particles that follow the fluid perfectly. Such tracer particles should never collide if the flow were incompressible, but given two swarms of tracer particles at different positions within the same grid cell and with a fluid velocity gradient over this cell, these two swarms will now have different velocities if interpolation is used to find the fluid velocity at the exact position of the particles. Since the swarms are filling the entire volume of the grid cell, this means that the two swarms will have different velocities and exist in the same volume, and hence, the swarms may collide. The larger grid cells yield potentially larger velocity differences between the particles, which explains why the coagulational growth is larger for the coarser resolutions. When NGP mapping is adopted, the artificial speedup disappears, as shown in the inset of Figure 7. Here, we used $N_p/N_{\rm grid} \approx 5$, which is appropriate based on Figure 4.

Next, we must ask how well the Eulerian models converge. As we have seen, for gravitational coagulation, the evolution of $\overline{r}$ is well converged at early times, while at later times, higher MBR only leads to *smaller* values of $\overline{r}$; see Figure 3. This makes the differences between Eulerian and Lagrangian approaches even larger and does therefore not contribute toward resolving the discrepancy between both approaches at early times. This is also true in the present case, as will be shown below.

We recall that there are no self-collision in the usual Smoluchowski scheme. The potential importance of this can be assessed by comparing with calculations in which self-collision is included either via methods (i) or (ii); see the end of Section 2.5 for their definitions. It turns out that by taking self-collision into account, method (i) causes only a weak speed-up in the increase of $\overline{r}$; see Figure 8. This is due to the fact that the number of potential collisional pairs with the same size is small and the kinematic straining flow cannot redistribute cloud droplets sufficiently. With method (ii), on the other hand, we find a strong enhancement of the growth. However, although method (ii) consists of an artificial manipulation of the diagonal terms of K_{ij}, it does not prove that self-coagulation is important, because similar manipulations of the off-diagonal terms of K_{ij} can have the same effect. In any case, this unphysical approach does not provide a proper solution to the convergence problem. We emphasize here that in the present Smoluchowski model with a maximum radius bin of 1 mm, be begin to lose mass at the largest mass bin. This is shown in the lower left panel of Figure 8.

In Figure 8 we also plot the evolution of the ratio of total droplet mass to gas mass, $M/m \equiv \sum\langle m\hat{f}\rangle/\langle\rho\rangle$, which is related to a_3. It turns out that this ratio starts dropping below the initial value when the largest radius bins ($a_{\rm max} = 10^{-3}$ m) begin to be populated. This is also seen from the evolution of a_{24}, which characterizes the maximum radius that is populated. Its value reaches

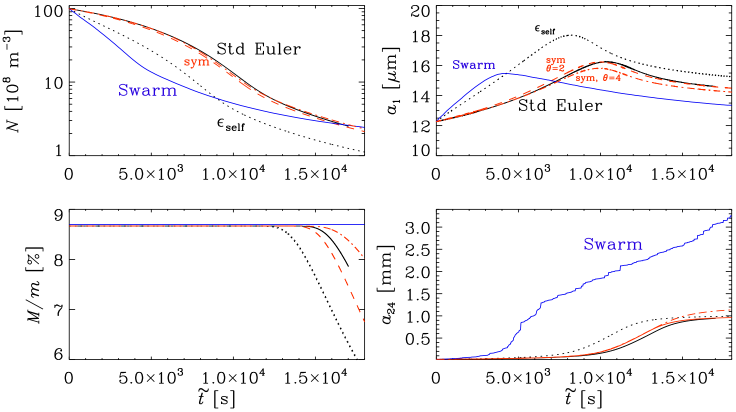

Figure 8: Comparison of purely collisional growth for Eulerian models with average self-collision (ϵ_{self}) and symmetric self-collision (red dashed for $\theta = 2$ and red dash-dotted for $\theta = 4$), as well as the swarm model in a kinematic straining flow. Here, $u_{\mathrm{rms}} = 0.7\,\mathrm{m\,s^{-1}}$, $\tau_{\mathrm{cor}} = 1.4\,\mathrm{s}$, while $\tau_{\mathrm{coag}} \approx 100\,\mathrm{s}$. The side length of the 2-D squared domain is $L = 2\pi\,\mathrm{m}$. The parameters of the Euler model are $k_{\mathrm{max}} = 53$, $n_0 = 10^{10}\,\mathrm{m}^{-3}$, $r_1 = 4\,\mu\mathrm{m}$, and $r_{\mathrm{ini}} = 12\,\mu\mathrm{m}$. Those for the swarm model are $N_p = 50000$ and NGP mapping is employed.

a saturation when $\tilde{t} \geq 10,000$.

3.3.2. *Combined condensation and coagulation*

When both condensation and coagulation play a role, it is no longer possible to define a unique timescale, and the solution depends on both τ_{cond} and τ_{coag}. We consider here the kinematic straining flow using $r_{\mathrm{ini}} = 12\,\mu\mathrm{m}$, $G = 5\times10^{-11}\,\mathrm{m^2/\,s}$ and $S = 0.01$, which yields $\tau_{\mathrm{cond}} = 144\,\mathrm{s}$. We investigate the role that particle viscosity and Brownian diffusion play in simulations using the Eulerian model. The Brownian motion of the particles is usually small, so the particle diffusion coefficient D_p should be finite but small. Since it is assumed that the particle flows are relatively dilute, there should be very little interaction between the different particle fluids, except of course for the occasional collisions. This implies that the particle viscosity ν_p should be close to zero[2]. For the Smoluchowski approach, both ν_p and D_p have to be made large in order to stabilize the simulations in spatially extended cases. It turns out that the values of these diffusion coefficients have a surprisingly strong effect on the solutions, which is shown in Figure 9. The inset shows that $\tau_{\mathrm{coag}} \approx 100$, which is comparable to τ_{cond} and both are long compared with $\tau_{\mathrm{cor}} \approx 1.4$. However, $\tilde{\tau}_{\mathrm{coag}} \approx 10,000$ is larger still.

Comparing now with the swarm approach, which avoids artificial viscosity and enhanced Brownian diffusion altogether, we see from Figure 9 that Eulerian and Lagrangian approaches

---

[2] Note that the particle viscosity represents the coupling between the particle fluids – not the drag coupling between the particles and the gas phase.

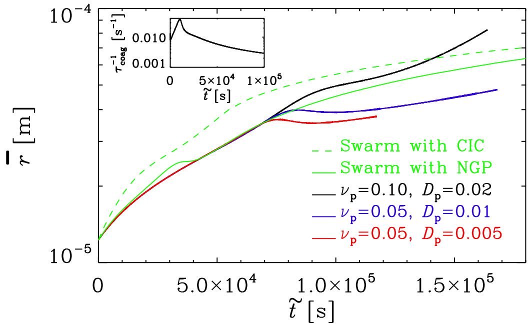

Figure 9: Evolution of $\bar{r}$ in a kinematic straining flow with combined condensation and coagulation. The different lines correspond to different amounts of artificial viscosity and enhanced Brownian diffusivity. The initial mean radius, supersaturation and condensation parameter is given by $r_{\rm ini} = 12\,\mu$m, $S = 0.01$ and $G = 5 \times 10^{-11}$ m^2/ s, respectively. $\theta = 2$ and $k_{\max} = 53$.

agree with each other at early times and follow the same trend at later times. This suggests that condensation has a “regularizing” effect and makes the overall evolution of $\bar{r}$ much less dependent on model details, which is due to the fact that the condensation process with constant positive supersaturation value leads to narrow size spectra of cloud droplets.

Another interesting aspect is the bump in the evolution of the mean radius. At first glance it seems counterintuitive that $\bar{r}$ can actually decrease during some time interval. However, as explained in detail in Appendix B, this can happen when the coagulation changes from primarily smaller particles coalescing to primarily larger particles coalescing. This is similar in the turbulent case, which will be discussed below. The peak appears earlier in the swarm model than in the Euler model. This may be due to the fact that the swarm model avoids the artificially enhanced diffusivity. Figure 9 shows that the peak appears earlier with decreasing viscosity and Brownian diffusion. Considering the extreme case that the viscosity and Brownian diffusion of the Eulerian model approaches zero, the results using both models should agree with each other. However, owing to the absence of a pressure term for particles, discontinuities would develop in the Eulerian model that destabilize the code if the viscosity and Brownian diffusion are too small. Again, this may be a strong argument in favor of using the swarm model for studying the collisional growth of cloud droplets.

3.4. Growth of droplets in 2-D turbulence

Turbulence is generally believed to help bridging the size gaps in both cloud droplet and planetesimal formation. In this section, turbulence-generated collisions are simulated using both the Eulerian and Lagrangian models. We consider a 2-D squared domain of side length $L = 0.5$ m at a resolution of 512^2 meshpoints, with viscosity $\nu = 5\times10^{-4}$ m^2 s^{-1} (which is about 50 times the physical value for air), average forcing wavenumber $k_{\rm f} \approx 40$, i.e., $k_{\rm f}L/2\pi \approx 3$, root-mean-square velocity $u_{\rm rms} = 0.8$ m s^{-1}, resulting in a Reynolds number of Re $= u_{\rm rms}/\nu k_{\rm f} \approx 40$. Our choice of $k_{\rm f}L/2\pi \approx 3$ corresponds to forcing at large scales that are not yet too large to be affected by

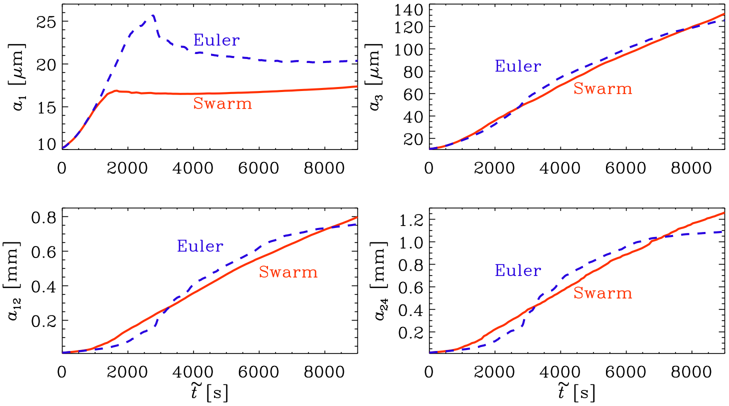

Figure 10: Comparison of a_1 (upper left), a_3 (upper right), a_{12} (down right) anda_{24} (down left) between the Eulerian model (dashed line) and the swarm model (solid line) with coagulation scheme II in 2-D turbulence.

constraints resulting the Cartesian geometry. The rate of energy dissipation per unit volume is $\epsilon = 2\nu\langle \mathbf{S}^2\rangle \approx 0.1\,\mathrm{m}^2\,\mathrm{s}^{-3}$ and the turnover time is $\tau_{\mathrm{to}} = (u_{\mathrm{rms}}k_{\mathrm{f}})^{-1} \approx 0.03\,\mathrm{s}$. For the Lagrangian model, we use NGP mapping while for the Eulerian model we adopt artificial viscosity and enhanced Brownian diffusivity for the particles ($\nu_{\mathrm{p}} = D_{\mathrm{p}} = 10^{-3}\,\mathrm{m}^2\,\mathrm{s}^{-1}$).

We first compare the evolution of the mean radius using both the Eulerian and Lagrangian models. As shown in Figure 10, the $\overline{r}$ agree well with each other at early times ($\tilde{t} < 1000\,\mathrm{s}$), after which they depart from each other, but follow the same trend. We emphasize that the collision process in a turbulent environment is strongly nonlinear. Thus, the agreement between the swarm model and the Euler model gives us a sense of the accuracy of the solution. It is worth noting that the MBR convergence of the Smoluchowski equation depends on the flow pattern. MBR shows strong discrepancies for gravitational coagulation, but a relatively weak dependence in the straining flow and converges at $k_{\mathrm{max}} \approx 55$ in turbulence.

In addition to inspecting the evolution of mean radius, More detailed insight can be gained by inspecting the evolution of size spectra as well as its high moments. Figure 11 shows a comparison of size spectra for the swarm and Eulerian models. The agreement of the spectra for both schemes is good for smaller particles until $\tilde{t} = 1000\,\mathrm{s}$. Moreover, the agreement of high moments (Figure 10) between the Eulerian model and the Lagrangian is good in turbulence. The reason why the higher moments of the Eulerian simulations flatten out for $\tilde{t} > 6000\,\mathrm{s}$ is that particles are lost through the upper mass-bin boundary.

We emphasize that for the swarm model, the interpolation scheme of the tracked swarms does affect the results, but this does not seem to be the case for turbulence. Turbulence continues to mix particles all the time while the straining flow tends to sweep up particles into predetermined locations that do not change. We may therefore conclude that the restriction on the interpolation scheme depends on the spatio-temporal properties of the flow. Nevertheless, a higher order

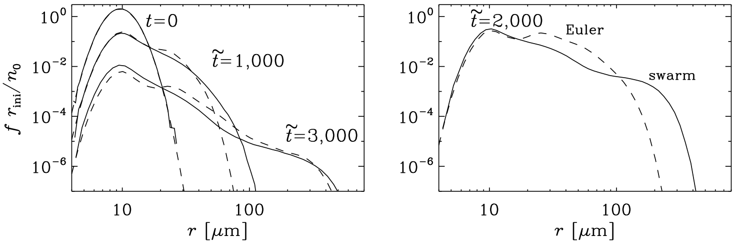

Figure 11: Comparison of size spectra for Lagrangian (solid lines) and Eulerian (dashed lines) approaches at different times in the presence of 2-D turbulence and no gravity nor condensation for the same run as shown in Figure 10. The largest departure between both approaches occurs for $\tilde{t}$ = 2000 s and is plotted separately in the right-hand panel.

interpolation is strictly not applicable to the swarm model.

The combined condensational and collisional growth in turbulence is investigated as well. Again, the results are similar to the case with pure collisional growth due to the fact that the condensation process in the present study with constant supersaturation is homogeneous. In future studies, the turbulence effect on the condensational growth should be considered, similar to what was done previously [24, 25].

4. Conclusion

The combined collisional and condensational growth of cloud droplets is studied in numerical simulations where the gas phase is solved on a mesh, while the particle phase is approximated by a point particle approach and is treated either by an Eulerian or a Lagrangian formalism. Our work extends previous work that investigated the condensation and collision processes individually [26, 27]. It is found that the Lagrangian approach agrees well with the analytic solution of condensational growth. By contrast, the Eulerian approach requires high resolution in the number of mass bins to avoid artificial speedup of the growth rate, which agrees with previous findings [13, 14]. It is worth noting that the MBR dependency is closely related to the temporal and spatial properties of the flow. The dependency is the strongest for gravity, less strongly for the straining flow, and weak for turbulence.

A detailed comparison of the collisional size spectra between the Lagrangian and Eulerian models demonstrates consistency between the two, especially when both condensation and coagulation are included. This suggests that condensation has a regularizing effect and makes the overall evolution of the mean radius less dependent on details such as the precise form of the initial condition or discretization errors that might affect the early evolution. However, the evolution of the mean radius, i.e., the ratio of the two lowest (first and zeroth) moments of the size distribution function, is a rather sensitive measure of particle growth. This is also seen in the fact that the mean particle radius often increases by not much more than a factor of three, while the size distribution can become rather broad and even millimeter-sized particles can be produced within a relatively short time. The mean particle radius is also not the most relevant one in that it does not characterize properly the growth of the largest particles. In fact, as we have shown in Appendix B, the mean radius actually *decreases* when two large particles collide. This is somewhat counterintuitive, but actually quite natural. When two very small particles coalesce, the sum of all radii does basically not change, but the number of particles decreased by one, so the average increases. By contrast, when two large particles coalesce, the particle number again decreases by one, but the sum of the radii decreases from 2 to $2^{1/3} \approx 1.26$, so the average also decreases.

When studying pure condensation, the Eulerian approach yields satisfactory results only when the mass bins are sufficiently fine. Furthermore, for non-gravitational (inhomogeneous) collisions, it is found that the Eulerian approach requires artificially large viscosity and Brownian diffusivity for keeping the resulting shocks in the particle fluid resolved. Because of this, it seems that for future studies of the effect of turbulence on condensational and coagulational growth of particles, the Lagrangian swarm approach would be most suitable. However, several precautions have to be taken. First, the symmetric coagulation scheme II [11] is to be preferred because it shows less scatter in the mean radius than the asymmetric scheme I. This is because in scheme I the particle number is adjusted to keep the total mass in the swarm constant. Second, when interpolation of the gas properties at the position of each Lagrangian particle is invoked (for example the CIC algorithm or the triangular shaped cloud scheme), both coagulation schemes yield artificially increased coagulation rates. This is because two swarms within the same grid cell may always collide since the interpolation of the fluid velocity results in a velocity difference between the two swarms. This causes a speedup of the coagulation rate already at early times. At larger grid resolution, the interpolated velocity differences are smaller, which reduces the coagulational growth. Therefore, it is best to map the gas properties to just the nearest grid point, which is found to yield converged results even at low resolution.

A shortcoming of the Smoluchowski model is that self-collisions are impossible. This should be mitigated by using finer mass bins, but it turns out that finer mass bins do not change the coagulation rate at early times, but rather decrease it at later times. This indicates that the contribution of self-collisions to the coagulation rate is relatively small.

The discrepancy between Lagrangian and Eulerian particle descriptions is particularly strong in the time-independent straining flow. This is because particles tend to be swept into extremely narrow lanes, which leads to high concentrations that can never be achieved with the Eulerian approach, in which sharp gradients must be smeared out by invoking artificial viscosity and large Brownian diffusivity. On the other hand, we are here primarily interested in turbulent flows that are always time-dependent, which limits the amount of particle concentration that can be achieved in a given time. In that case, the discrepancies between Eulerian and Lagrangian approaches are smaller at early times, but there are still differences in the evolution of the mean radius at late times. This can easily be caused by changes in the relative importance of collisions of large and small particles. This is confirmed by the fact that the size distribution spectra in the turbulent case are more similar for Lagrangian and Eulerian approaches than in the straining flow.

Our present work neglects local and temporal changes in the supersaturation ratio. In future studies, we will take into account that the supersaturation ratio increases (decreases) as a fluid parcel rises (falls). We would then be able to account for the fact that the total water content should remain constant and that the supersaturation ratio would become progressively more limited as water droplets grow by condensation. Another important shortcoming is our assumption of perfect collision efficiency, which resulted in artificially rapid cloud droplets growth. Alleviating these restrictions will be important tasks for future work. Furthermore, we have here only considered 2-D turbulence. Extending our work to 3-D is straightforward, but our conclusions regarding the comparison of different schemes should carry over to 3-D.

Appendix A. Upwinding scheme for a nonuniform mesh

In the presence of condensation alone, the evolution equation for $f(r,t)$ as a function of radius r and time t is given by

$$\frac{\partial f}{\partial t} = -\frac{\partial}{\partial r}(fC), \tag{A.1}$$

where $C \equiv \mathrm{d}r/\mathrm{d}t$ and is given by Eq. (5). Thus, we have

$$\frac{\partial f}{\partial t} = -A\frac{\partial}{\partial r}\left(\frac{f}{r}\right) \tag{A.2}$$

where $A = GS$ is assumed independent of r; see Eq. (13.14) of [28]. Is can be seen from the form of the analytic solution that there will be a discontinuity at $r^2 = 2At$, which is numerically difficult to handle. In particular, it is difficult to ensure the positivity of f. For these reasons, a low-order upwind scheme is advantageous. Furthermore, expanding the RHS of Eq. (A.2) using the quotient rule,

$$\frac{\partial f}{\partial t} = \frac{A}{r^2}f - \frac{A}{r}\frac{\partial f}{\partial r}, \tag{A.3}$$

it is obvious that the first term in isolation would lead to exponential growth of f proportional to $\exp(At/r^2)$, which must be partially canceled by the second term. If the cancellation is numerically imperfect, $f(r,t)$ will indeed grow exponentially, which tends to occur in regions where $r^2 < 2At$, i.e., where f should vanish. For nonuniform mesh spacing, r_k with $k = 1, 2, ..., k_\mathrm{max}$, the first-order upwind scheme can be written as

$$\frac{\partial f_k}{\partial t} = c_k^+\frac{f_{k+1}}{r_{k+1}} + c_k^0\frac{f_k}{r_k} + c_k^-\frac{f_{k-1}}{r_{k-1}} \tag{A.4}$$

with

$$c_k^\pm = \pm\tfrac{1}{2}\frac{|A| \mp A}{r_{k\pm1} - r_k}, \quad c_k^0 = -c_k^+ - c_k^-. \tag{A.5}$$

On the boundaries of the radius bins at $k = 1$ and k_max, Eq. (A.4) cannot be used unless we make an assumption about the nonexisting points outside the interval $1 \le k \le k_\mathrm{max}$. For example, for $k = k_\mathrm{max}$, the coefficient c_k^+ would multiply f_{k+1}/r_{k+1}, which is not defined. Therefore, a simple assumption is to set $c_k^+ = 0$. However, c_k^+ also enters in the expression for c_k^0, which is the factor in front of f_k/a_k. The coefficient c_k^+ can only be nonvanishing when $A < 0$. If we were to omit c_k^+ in the expression for c_k^0, then, for $A < 0$, the value of f_k would not evolve at $k = k_\mathrm{max}$ and would be frozen. Thus, the non-existing points lead to an unphysical situation. It would be natural to assume that at $k = k_\mathrm{max}$, f_k should decay with time at a rate $-(|A| - A)/r_k$. Therefore, assume

$$c_k^+ = 0, \quad c_k^0 = -(|A| - A)/r_k - c_k^- \quad (\text{for } k = k_\mathrm{max}) \tag{A.6}$$

and c_k^- unchanged, and analogously

$$c_k^- = 0, \quad c_k^0 = -(|A| + A)/r_k - c_k^+ \quad (\text{for } k = 0) \tag{A.7}$$

and c_k^+ unchanged.

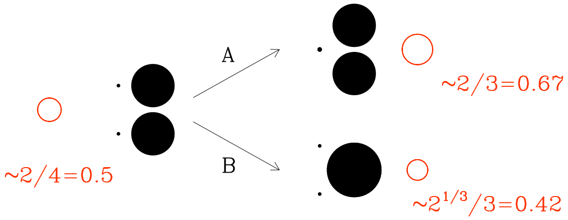

Figure B.12: Sketch illustrating the growth of $\bar{r}$ when two small particles coalesce (A) and the decrease of $\bar{r}$ when two large particles coalesce (B). Filled black symbols denote actual particle sizes and open red symbols and red text refer to $\bar{r}$.

Appendix B. The "peak" in the evolution of the mean particle radius

For the following discussion, it is convenient to introduce the moments

$$M_\zeta = \sum f(r)\, r^\zeta. \tag{B.1}$$

so that $a_\zeta = (M_\zeta/M_0)^{1/\zeta}$ and $\bar{r} = a_1$, as before. Let us now assume a situation with pure coagulation such that the total volume of water in the droplets is conserved. This implies that M_3 is constant, while M_0 and M_1 will always decrease with time. However, the relative rates at which M_0 and M_1 decrease can change. Indeed, a peak in $\bar{r}$ is observed if M_1 switches from decreasing more slowly with time than M_0 to decreasing faster than M_0. An example of such a situation will be presented in the following.

For a flow with two small and two large particles, with radii r_S and r_L, respectively, the size distribution is given by $f(r) = 2\delta_{r r_\mathrm{S}} + 2\delta_{r r_\mathrm{L}}$, where δ_{ij} denotes the Kronecker delta ($\delta_{ij} = 1$ for $i = j$ and 0 otherwise). From Eq. (B.1) it can then be found that the initial number of particles and sum of particle radii is given by $M_0(0) = 4$ and $M_1(0) = 2r_\mathrm{S} + 2r_\mathrm{L}$, respectively. This yields a mean initial particle radius of $\bar{r}(0) = M_1(0)/M_0(0)$. In the following, we assume that $r_\mathrm{S} \ll r_\mathrm{L}$, so that $\bar{r}(0) \approx r_\mathrm{L}/2$.

When two particles of radius r_0 coalesce, their combined mass is unchanged, so $2r_0^3 = r^3$, i.e., the target radius becomes $r = 2^{1/3} r_0$. Let us now consider two different collision scenarios; cf. Figure B.12. In scenario A, two smaller particles coalesce such that $M_0(\mathsf{A}) = 3$ and $M_1(\mathsf{A}) = 2^{1/3} r_\mathrm{S} + 2r_\mathrm{L}$, while in scenario B two larger particles coalesce such that $M_0(\mathsf{B}) = 3$ and $M_1(\mathsf{B}) = 2r_\mathrm{S} + 2^{1/3} r_\mathrm{L}$. Since $r_\mathrm{L} \gg r_\mathrm{S}$, we find for $\bar{r}$ in both scenarios

$$\bar{r}(\mathsf{A}) = (2^{1/3} r_\mathrm{S} + 2r_\mathrm{L})/3 \approx 2r_\mathrm{L}/3 \approx 0.67 r_\mathrm{L} > \bar{r}(0), \tag{B.2}$$

$$\bar{r}(\mathsf{B}) = (2r_\mathrm{S} + 2^{1/3} r_\mathrm{L})/3 \approx 2^{1/3} r_\mathrm{L}/3 \approx 0.42 r_\mathrm{L} < \bar{r}(0). \tag{B.3}$$

This means that for scenario A the mean particle radius is increasing, while for scenario B it is decreasing. When a peak appears in the time evolution of the mean particle radius, this then typically means that it is primarily the heavier particles that are coalescing.

Acknowledgments

We thank Nathan Kleeorin, Dhrubaditya Mitra, and Igor Rogachevskii for useful discussions. This work was supported through the FRINATEK grant 231444 under the Research Council of Norway, the Swedish Research Council grant 2012-5797, and the grant “Bottlenecks for particle growth in turbulent aerosols” from the Knut and Alice Wallenberg Foundation, Dnr. KAW 2014.0048.

References

[1] R. A. Shaw, *Ann. Rev. Fluid Mech.* **35**, 183 (2003).
[2] W. W. Grabowski and L.-P. Wang, *Ann. Rev. Fluid Mech.* **45**, 293 (2013).
[3] M. B. Pinsky and A. P. Khain, *Quart. J. Roy. Met. Soc.* **123**, 1517 (1997).
[4] G. Falkovich, A. Fouxon, and M. G. Stepanov, *Nature* **419**, 151 (2002).
[5] N. Riemer and A. S. Wexler, *J. Atmosph. Sci.* **62**, 1962 (2005).
[6] A. Johansen, J. S. Oishi, M.-M. Mac Low, H. Klahr, T. Henning, and A. Youdin, *Nature* **448**, 1022 (2007).
[7] A. Johansen, A. N. Youdin, and Y. Lithwick, *Astron. & Astrophys.* **537**, A125 (2012).
[8] Y. Ogura and T. Takahash, *J. Atmosph. Sci.* **30**, 262 (1973).
[9] G. Svensson and J. H. Seinfeld, *Quart. J. Roy. Met. Soc.* **128**, 535 (2002).
[10] H. R. Pruppacher and J. D. Klett, *Microphysics of Clouds and Precipitation: Reprinted 1980*, Springer Science & Business Media, 2012.
[11] S. Shima, K. Kusano, A. Kawano, T. Sugiyama, and S. Kawahara, *Quart. J. Roy. Met. Soc.* **135**, 1307 (2009).
[12] Zsom, A. and Dullemond, C. P., *Astron. & Astrophys.* **489**, 931 (2008).
[13] K. Ohtsuki, Y. Nakagawa, and K. Nakazawa, *Icarus* **83**, 205 (1990).
[14] J. Drążkowska, F. Windmark, and C. P. Dullemond, *Astron. & Astrophys.* **567**, A38 (2014).
[15] N. P. Sullivan, S. Mahalingam, and R. M. Kerr, *Phys. Fluids* **6**, 1612 (1994).
[16] D. Lamb and J. Verlinde, *Physics and Chemistry of Clouds*, Cambridge, England, Cambridge Univ. Press, 2011.
[17] G. Suttner and H. W. Yorke, *Astrophys. J.* **551**, 461 (2001).
[18] A. Johansen, *Ice condensation, dust coagulation and vortex activity in protoplanetary discs*, Master’s thesis, Univ. Copenhagen, 2004.
[19] N. E. L. Haugen, A. Brandenburg, and W. Dobler, *Phys. Rev. E* **70**, 016308 (2004).
[20] A. Johansen, A. C. Andersen, and A. Brandenburg, *Astron. & Astrophys.* **417**, 361 (2004).
[21] N. Babkovskaia, M. Boy, S. Smolander, S. Romakkaniemi, U. Rannik, and M. Kulmala, *Atmosph. Res.* **153**, 49 (2015).
[22] J. H. Seinfeld and S. N. Pandis, *Atmospheric chemistry and physics: from air pollution to climate change*, John Wiley & Sons, New Jersey, 2006.
[23] P. G. Saffman and J. S. Turner, *J. Fluid Mech.* **1**, 16 (1956).
[24] B. Kumar, J. Schumacher, and R. A. Shaw, *J. Atmosph. Sci.* **71**, 2564 (2014).
[25] G. Sardina, F. Picano, L. Brandt, and R. Caballero, *Phys. Rev. Lett.* **115**, 184501 (2015).
[26] M. Simmel, T. Trautmann, and G. Tetzlaff, *Atmosph. Res.* **61**, 135 (2002).
[27] M. Simmel and S. Wurzler, *Atmosph. Res.* **80**, 218 (2006).
[28] J. H. Seinfeld, *Atmospheric chemistry and physics of air pollution*, Cambridge, England, Cambridge Univ. Press, 1998.